

A Cam-Based Inchworm Robot for Pipe Traversal

MECH5845M Professional Project

**A Cam-Based Inchworm Robot for
Pipe Traversal**

Author: Thomas Milner 201397578

Supervisor: Dr George Jackson-Mills

Examiner: Dr Robert Richardson

Date: 07/08/25



UNIVERSITY OF LEEDS

**SCHOOL OF MECHANICAL
ENGINEERING**

MECH5845M Professional Project

TITLE OF PROJECT

A Cam-based Inchworm Robot for Pipe Traversal

PRESENTED BY

Thomas Milner

If The Project Is Industrially Linked Tick This Box
And Provide Details Below

Company Name and Address:

This project report presents my own work and does not contain any unacknowledged work from any other sources.

Signed

A handwritten signature in blue ink that appears to read "Thomas Milner".

date: 07/08/25

Contents

List of Figures	v
List of Tables	vii
Nomenclature	viii
Abstract	ix
1 Introduction	1
1.1 Introduction	1
1.2 Aims	2
1.3 Objectives	2
1.4 Project Report Layout	2
2 Literature Review	3
2.1 Introduction	3
2.2 Cable Ducts and Draw Rope	3
2.2.1 Vacuum Blower	3
2.2.2 Duct Rod	4
2.2.3 Robotics	4
2.3 Pipe Traversal Robotics	4
2.3.1 Wheeled Robots	4
2.3.2 Tracked Robots	5
2.4 Inchworm Locomotion	5
2.4.1 Principle of Operation	5
2.4.2 Elongation and Contraction (EC) Mechanism	6
2.4.3 Wall Gripping and Releasing (GR) Mechanism	8
2.5 Cylindrical Cams	10
2.5.1 Principle of Operation	10
2.5.2 SVAJ Diagrams	11

2.5.3	Rises, Dwells, and Returns	11
2.6	Summary	12
3	Cylindrical Cam Design	13
3.1	Introduction	13
3.2	Cylindrical Cam	13
3.3	Design	13
3.3.1	Cycloidal Curves	13
3.3.2	Cam Path Generator	14
3.3.3	Fusion Design	15
3.3.4	Reducing Moments	16
3.3.5	Design for Manufacturability and Assembly	17
3.3.6	3D Printing	17
3.3.7	Tolerances	18
3.4	Testing	18
3.4.1	Velocity Tests	18
3.4.2	Displacement Tests	19
3.5	Discussion	19
4	Inchworm Prototype	21
4.1	Introduction	21
4.2	Inchworm Chassis	21
4.2.1	Integrated Linear Bearing	22
4.2.2	Assembly	22
4.3	Initial Velocity Tests	22
4.3.1	Setup	22
4.3.2	Methodology and Results	23
4.3.3	Analysis	23
4.4	Bristle Assembly Friction Coefficients	24
4.4.1	Bristle Friction	24
4.4.2	Setup	24

4.4.3	Methodology	24
4.4.4	Limitations	25
4.4.5	Results	25
4.4.6	Analysis	26
4.5	Motor Selection	26
4.5.1	Torque Profiles	26
4.5.2	Cam Torque	26
4.5.3	Motor Torque	27
4.6	Real World Testing - BT Adastral	29
4.6.1	Setup	29
4.6.2	Methodology and Results	29
4.6.3	Analysis	30
4.7	Discussion	30
5	Conclusion	31
5.1	Achievements	31
5.2	Discussions	31
5.3	Conclusions	32
5.4	Future Work	32
References		33
A	Integrated Linear Bearing Testing	36
B	Inchworm Prototype Assembly	37
C	Slipping Bristles	38
D	Cam Curve Comparison	39
D.1	Sine Squared	39
D.2	Polynomial Cam Curve	40
E	Inchworm Comparison	41

List of Figures

2.1 Principle of Inchworm Locomotion.	5
2.2 An example bristle assembly constructed from PVC bristles and “Tough 2000” [38] resin	9
2.3 Bristle assembly providing the grip/release mechanism through anisotropic friction.	10
2.4 Existing bristle assemblies	10
2.5 Cylindrical Cam [39]	10
2.6 Cam SVAJ Diagram	11
2.7 Examples of Cam Follower Motion, characterised with Rise, Dwell and Return phases [41].	12
3.1 Elongate Contract mechanism.	13
3.2 SVAJ plot generated by the Cam Path Generator	15
3.3 Designing a cam from the cycloidal curve	16
3.4 Two identical, in-phase cams stacked along the cam shaft axis and rotated 180° to cancel out their moments on the cam shaft.	16
3.5 Cam assembly process	17
3.6 3D printed cam parts and ball bearings, lubricated.	18
3.7 Cam mounted on Dewalt drill.	19
3.8 Measuring the cam stroke length L at different cam shaft angles.	19
4.1 (A) Inchworm prototype design. (B, C) Threaded inserts for bristle attachments.	21
4.2 Closed inchworm robot, secured with locking rings.	22
4.3 Cross section of integrated linear bearing.	22
4.4 First functional prototype of the inchworm, integrating the motor, cylindrical cam, and bristle assemblies.	22
4.5 Footage of inchworm velocity test, aswell as theoretical vs measured inchworm velocities.	23
4.6 Newton meter measuring the F_B coefficient of a bristle assembly	24
4.7 Measurements of static friction coefficients of various bristle assemblies	25

4.8	Inchworm with Assembly C	25
4.9	Cam torque plot generated by Cam Path Generator	27
4.10	Torque profiles of various motors vs the cycloidal cam. The optimal motor can be seen to be motor (D), as it provides the highest average operating RPM.	28
4.11	BT OpenReach fibre optic cable duct testbed, featuring two 3m x 50mm ID cable ducts connected by a spigot and socket joint.	29
4.12	Inchworm prototype stuck in the spigot and socket pipe joint	29
A.1	Testing the linear bearing subassembly. The cam shaft is rotated, causing the cam follower to reciprocate, whilst the housing remains stationary.	36
B.1	(A) The inchworm mid-assembly. (B,C) Threaded inserts for attaching bristle assemblies.	37
C.1	Bristle assemblies slipping during the elongation phase.	38
D.1	Sine Square Cam SVAJ.	39
D.2	Polynomial Cam SVAJ.	40

List of Tables

4.1 Construction and performance of different bristle assemblies.	26
E.1 Comparison of the cam-based inchworm robot against other inchworms in the literature.	41

Nomenclature

EC - Elongation and Contraction Mechanism

GR - Gripping and Release Mechanism

AF - Anisotropic Friction

Abstract

The project aimed to produce an inchworm robot capable of pulling draw rope through small (50 mm internal diameter) fibre-optic cable ducts. The project objectives were to (O1) develop a workflow for the rapid design of miniature cylindrical cams, (O2) design and test a prototype cam, (O3) use the cam to create an inchworm prototype, and (O4) evaluate and optimise the robot's velocity.

A literature review identified cylindrical cams as a promising elongation/contraction (EC) mechanism due to their potential for high speeds, and “bristle assemblies” as an effective passive anisotropic friction-based grip/release (GR) mechanism.

A Python-based “Cam Path Generator” was developed to generate and analyse SVAJ plots of supplied cam curve equations, and provide operating torque estimations. A cylindrical cam workflow was developed and successfully tested, and an inchworm robot constructed using the aforementioned EC and GR mechanisms. The cylindrical cam, bristle assemblies and motor were optimised for velocity, achieving a maximum velocity of 25.5 mm and surpassing comparable inchworm robots in the literature.

Real-world testing showcased the inchworm’s ability to drag a 14.5g draw rope through 6m of pipe, although work remains to navigate socket and spigot pipe connections.

The study concludes that cylindrical cam actuation, combined with passive anisotropic friction-based bristle assemblies, offers a fast, small approach for pipe traversal robotics.

1 Introduction

1.1 Introduction

Fibre optic cables allow high speed communications across large distances and are the backbone of the internet [1]. “BT Openreach” [2] provide one of the largest fibre optic broadband networks in the UK, and are aiming to provide 25 million homes with fibre optic broadband by the end of 2025 [2] by installing fibre-optic connections directly into people’s homes. This is known as fibre-to-the-premises, or FTTP [2].

To install FTTP, fibre optic cables are installed in underground ducts leading to the premises. Openreach ducts have an internal diameter of either 50mm or 90mm and come pre-installed with a draw rope, which is a rope that spans the length of the inside of the pipe. To install a new fibre optic cable in a duct, the end of the cable is attached to the end of the draw rope, and the draw rope is used to pull the cable into the duct. One duct can carry multiple fibre optic cables, and when installing a cable, care must be taken to provide a new draw rope for the next cable to be installed.

This presents the problem; often, as cables are installed, draw ropes are pulled completely out of the duct. To easily lay future cables a new draw rope must be installed.

Installing draw ropes is hard work [3]. The market of existing tooling for laying draw ropes can be split into two categories: manual tools, that are labour intensive, cumbersome, and time-consuming, and automatic tools that are expensive and require complicated facilitating infrastructure. Due to either wage or equipment costs, both options are expensive.

Robotics present an attractive solution to draw rope laying. A draw rope laying robot could traverse the duct and lay the draw rope behind it, moving faster than existing tools, reducing the technician’s manual labour load, and freeing the technicians to perform other tasks, compounding the cost-saving effect.

Industry solutions for pipe traversal robotics are well established for large diameter (> 100 mm) pipes [4]–[6]. However, small diameter pipes (< 100 mm) remain a problem, likely due to the difficulty of fitting actuation mechanisms into the small space. Research on small diameter pipe traversal robotics can be categorised via locomotion method, such as wheels, legs, screws or inchworms [7]. Inchworm robots are an attractive solution due to their actuation principle suiting the space constraints of small pipes. However, they are often slow [8]; draw rope laying requires a fast robot in order to decrease the time (and thus, cost) required to lay a draw rope in a cable duct.

Cylindrical cams are well-documented mechanisms that provide fast linear motion. However, they are under-utilised in inchworm robotics likely due to the complex design and assembly processes required. 3D printing has the potential to ease the design and assembly of small cylindrical cams due to its ability to manufacture complex geometries

with sub-millimetre resolution [9].

This project develops a workflow to facilitate the design and integration of cylindrical cams into inchworm robotics using 3D printing, and details the construction and analysis of a prototype inchworm robot that utilises cylindrical cams and anisotropic friction to lay draw rope in 50mm diameter fibre optic cable ducts.

1.2 Aims

The project aim is to develop a cylindrical-cam-based inchworm robot capable of traversing a 3 metre length of pipe of 50 mm internal diameter, whilst towing a draw rope behind it.

1.3 Objectives

The project objectives are as follows:

- O1** Develop a workflow for rapid design and prototyping of cylindrical cams.
- O2** Design, assemble, and test a cylindrical cam created using the workflow.
- O3** Integrate the cylindrical cam into an inchworm robot.
- O4** Analyse the robot's performance and optimise it for velocity.

1.4 Project Report Layout

After this introductory chapter the report will review existing methods and tools (both manual and automated) for Openreach fibre optic cable laying. The review will then analyse the speeds of commercial solutions for pipe-traversal robotics, before exploring inchworm-style pipe robotics. Common actuation methods for driving inchworm robots will be reviewed and analysed with a focus on velocity and size to identify suitable technologies for producing a small, fast inchworm capable of laying draw rope. Cylindrical cams and anisotropic friction will be identified as potential solutions, and their principles of operation will be explored.

Next, the report will cover the development of a workflow to design and prototype cylindrical cams using 3D printing. The report will then detail the design, assembly, testing, and analysis of an inchworm robot constructed using the workflow. The report will also cover optimisations performed on the robot to improve its speed.

Finally, the report will cover testing the robot in a real-world environment to demonstrate its capabilities for laying draw rope in fibre optic cable ducts.

2 Literature Review

2.1 Introduction

The literature review covers background information on laying fibre optic cables in cable ducts using draw ropes, and the strengths and weaknesses of existing draw rope laying tools. The review then explores pipe traversal robotics as a solution for laying draw rope, and analyses existing solutions with a focus on velocity and size before identifying inchworm locomotion as a potential solution for a small-scale pipe traversal robot. The two driving mechanisms of an inchworm, elongate/contract and grip/release, are described, and solutions for each mechanism are discussed, resulting in the identification of cylindrical cams and anisotropic friction as two mechanisms that could successfully drive an inchworm robot. Finally, the review details some of the background theory behind cylindrical cam design, as this is where a large proportion of the project work lies.

2.2 Cable Ducts and Draw Rope

BT Openreach [2] provides fibre optic infrastructure across the UK. This includes cable ducts, which are underground pipes that provide safe passage to fibre optic cables between premises. Openreach cable ducts are available in two internal diameters, 90 mm and 50 mm [2], and upon installation a *draw rope* is installed within each pipe. A *draw rope* allows an operator to install a cable into a duct by attaching one end of the cable to the end of the draw rope, and using the rope to pull the cable into the duct. Draw rope is available in a variety of diameters, lengths and strengths to suit the requirements of the cables being installed [10].

If no draw rope is installed, operators can instead install the cable using a “cable blower”[11], which uses compressed air to “blow” the cable into the duct [12]. This is a costly and time-consuming process as complex machinery must be set up for each cable and the operator must have access to compressed air [12].

A more suitable method is to re-lay the draw rope, which can then be reused for all future cable installations. Common tools and techniques for laying draw ropes within ducts are as follows.

2.2.1 Vacuum Blower

The most inexpensive method of the selection, this involves attaching a “plug” (often a plastic bag) to the end of the draw rope and using a vacuum cleaner to pull the plug (with rope attached) through the length of the duct using air pressure [13]. Whilst this is effective for very short lengths of duct, the range of the method depends on the vacuum’s power, and an operator must be present throughout the process.

2.2.2 Duct Rod

A duct rod is a more manual approach, involving a flexible shaft (supplied on a reel) that an operator pushes through the length of the duct [14], [15], either by hand or using specialised machinery [16]. Once the rod is through the duct, the operator attaches a draw rope to the end of the rod, and pulls the rod back through the duct, installing the draw rope.

This method is especially effective in blocked or clogged ducts - the rigidity of the rod allows the operator to “pierce” blockages and clear a path for the draw rope. However, the rod reel is a large piece of equipment to transport, and the rodding process is either manual and labour intensive, or machine driven and expensive. Both methods require the operator’s full attention throughout the whole process.

2.2.3 Robotics

Robotics present an attractive solution to draw rope laying; by fully automating the laying process the operator’s time is freed up to complete other tasks. Multiple robots could lay draw ropes in multiple ducts in parallel, compounding the time-saving benefits.

There are minimal robotic solutions specifically designed for laying draw rope within ducts. However, there is a large amount of research on general in-pipe traversal robotics, also known as pipe crawlers.

2.3 Pipe Traversal Robotics

This section of the review explores existing locomotion methods for pipe traversal robotics and analyses them based on speed and size. The current fastest actuation methods for pipe robotics are wheel based robots and track-based robots [17]. As such, this review analyses some example speeds of such robots, in order to inform the target maximum velocity of the robot produced in this project.

2.3.1 Wheeled Robots

Wheeled robots provide high-speed movement, with Dertien and Stramigioli [18], Park et al [19], and Kakogawa et al [20] achieving speeds of 56mm/s, 30 mm/s, and 80 mm/s, respectively. The limitations of wheeled robots are their size and complexity. The smallest of the aforementioned robots (Dertien and Stramigioli) can traverse pipes of a minimum diameter of 63mm, larger than our 50mm target. The robots also involve assemblies consisting of multiple actuators and complicated mechanisms, increasing the robot’s cost. Thus, the literature suggests wheeled robots are unsuitable for the problem at hand, unless the underlying mechanisms can be minitaurised.

2.3.2 Tracked Robots

Tracked robots use caterpillar tracks for locomotion and share the same strengths and weaknesses as wheeled robots - they are fast, but large. Tracked robots have enjoyed success as commercial solutions for large-diameter pipeline inspection; the “Inuktun Versatrax” allows inspection of pipes of minimum diameter 102mm with a maximum speed of 150mm/s[5]. The “Synthotech SynthoTRAX” is even larger at 250mm minimum diameter, although its maximum velocity is not specified. It is clear that alike wheeled robots, caterpillar track based pipe traversal robots are very fast, but too large for this project.

2.4 Inchworm Locomotion

Wheeled and tracked pipe traversal robotics are fast, but large. This project aims to produce a robot capable of reaching comparable speeds, whilst remaining small enough to be used in small ($< 100\text{mm}$) diameter pipes. For this, inchworm locomotion has been chosen. Inchworm movement (also known as two-anchor crawling) is a locomotion method used by caterpillars [21]–[23], allowing in-line movement either forwards or backwards.]

2.4.1 Principle of Operation

The principle of operation of inchworm locomotion is as follows. An inchworm robot can be simplified into a front and back module (as shown in Figure 2.1), and the locomotion can be explained through the use of two submechanisms:

1. **Elongate/Contract (EC)**: responsible for moving the front and back modules further apart (elongate) and closer together (contract).
2. **Grip/Release (GR)**: responsible for allowing each module to either "grip" the surface (not able to move) or release the surface (able to move).

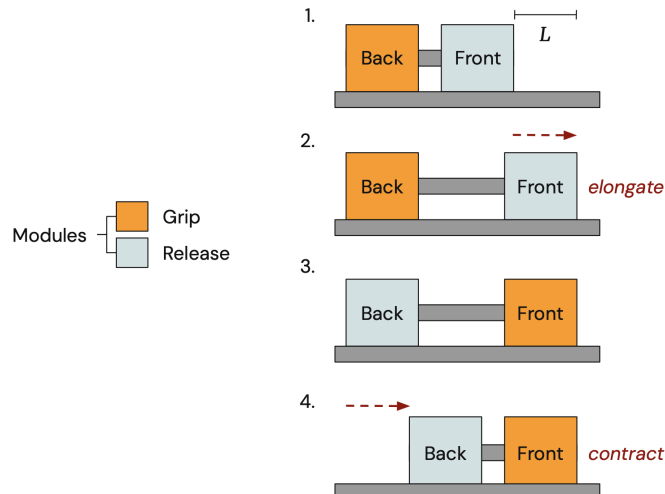


Figure 2.1: Principle of Inchworm Locomotion.

Each cycle of the mechanism consists of four steps, as illustrated in Figure 2.1:

1. The back of the robot grips the surface and the front releases.
2. The robot elongates, pushing the front of the robot forwards a distance L .
3. The front of the robot grips the surface, and the back of the robot releases.
4. The robot contracts, pulling the back of the robot towards the front.

At the end of each cycle, the robot has moved one stroke length (L) in the chosen direction. As the project aims to build a small, fast inchworm, a literature review is performed to identify actuation methods for each sub-mechanism that will enable a small, fast robot capable of towing a draw rope.

2.4.2 Elongation and Contraction (EC) Mechanism

Introduction

Unfortunately, most current inchworm robots are slow [8]. A significant contributor to an inchworm's speed is its elongate and contraction (EC) mechanism. This review explores common actuation methods used to provide elongation and contraction in inchworm robotics and aims to identify potential actuation mechanisms that could enable a fast inchworm robot.

Pneumatics

Pneumatics are a well-studied and popular actuation strategy for EC mechanisms in inchworm robotics. The majority of pneumatic solutions rely on custom-designed bellows integrated into the body of the inchworm robot that elongate when pressurised and contract when depressurised. Using custom pneumatic bellows, Miyasaka et al [24], Hayashi et al [25], and Peng et al [8], have produced inchworm movement capable of 24.2 mm/s, 14 mm/s, and 8.54 mm/s respectively, all with diameters < 50 mm, showing that pneumatic bellows can provide fast inchworm movement for small pipe robotics.

Luedtke et al [26] developed custom pneumatic bellows manufactured using 3D printing. Whilst the developed robot was slower than those previously mentioned (4.25mm/s), the research highlights how 3D printing could be a quick and effective manufacturing method for the mechanism.

Lin et al [27] utilise pneumatics differently by integrating a McKibben actuator to provide EC. A McKibben actuator is a type of Pneumatic Artificial Muscle (PAM) that contracts when pressurised [28], working the opposite way to the aforementioned pneumatic bellows. The PAM allowed the robot speeds of up to 27 mm/s, with operators able to adjust the speed of the robot by adjusting the time it took to inflate/deflate the McKibben actuator [27].

Pneumatics is thus a tempting solution for inchworm locomotion, as it allows higher speeds than most other inchworm actuators. However, the shortcomings of pneumatic

inchworms lie in the supporting infrastructure outside the pipe; all pneumatic solutions require a constant supply of air to provide the required pressure. This requires the operator to have access to an air supply and supporting equipment, vastly increasing the complexity of the draw-rope laying process. Operators will also need separate air lines to run multiple robots at once.

As such, despite being an attractive solution for the velocities it provides, pneumatics will not be suitable for this project as the supporting infrastructure required vastly increases the complexity of the solution - smaller, more easily controlled solutions are required.

Shape Memory Alloys (SMA)

In many robots [21], [29], [30], Shape Memory Alloy (SMA) wires are used to implement the EC mechanism. These are wires that will contract when a current is passed through them [31], allowing them to be controlled and powered by a simple electrical circuit. SMA wires are also small, allowing for small inchworm robot designs; Wang et al[21] utilised SMA wires to produce a robot only 63 g, with a diameter of 140 mm.

However, SMA wires are slow - the SMA-based inchworm robot developed by Wang et al[21] has a maximum speed of 3.5 mm/s. The aforementioned SMA-based robots are also fragile and could be easily damaged in rugged underground environments. As such, SMA wires are unsuitable for the project as although they are small, they are slow and too fragile.

Motor-based Linkages

Mechanical linkages that turn a rotational input into a linear output are well-documented and fast. Mechanisms such as crank-and-sliders, scotch yokes, lead screws, and cams are commonplace. However, they are not often seen in inchworm robotics, with designers often opting for more complex actuation mechanisms as described above.

The main reasoning behind this seems to be size. Xie et al [32] produced a robot that uses just one motor to provide both EC and GR mechanisms through the use of crank-slider and cam assemblies, but the robot's resulting diameter is 360 mm - far above this project's 50 mm limit.

Saab et al [33] use a crank-and-slider design in an inchworm to produce a robot capable of reaching 137.99 mm/s, highlighting the impressive speeds these mechanisms could produce. However, the robot has a maximum diameter of 76 mm, which is above the 50 mm target.

Miniaturising classic motor-based mechanisms using 3D printing seems an untapped research avenue in inchworm robotics. Commercial 3D printers can achieve resolutions of 0.08 mm [9], enabling the manufacture of small, complex mechanisms. Cylindrical cams are well documented as effective solutions for creating high-speed reciprocating

motion [34]; manufacturing cylindrical cams using 3D printing could result in a low-size, high-speed EC mechanism.

2.4.3 Wall Gripping and Releasing (GR) Mechanism

Introduction

To build a small, fast inchworm robot that is capable of towing a draw rope, the GR mechanism must be small, quick to actuate, and provide a strong “grip” force so that the robot doesn’t slip whilst towing the rope. Pneumatics are a common solution for implementing GR mechanisms [8], [24], [25]; however, the shortcomings of the supporting infrastructure have already deemed pneumatics unfit for the project. As such, the review turns to another common GR solution: anisotropic friction.

Anisotropic Friction

Anisotropic friction (AF) is direction-dependent friction [35] and is a common mechanism to provide a GR mechanism in inchworm robotics due to its ability to work at a small scale. Most AF solutions reviewed met the project size and speed criteria. As such, this section of the review analyses the anisotropic friction range ‘ f ’ provided by each mechanism, which is quantified as follows. Static friction in the forward direction is indicated as F_F , and friction in the backward direction is indicated as F_B . The anisotropic range f is the ratio $f = F_B/F_F$. An ideal inchworm AF mechanism will have a large f ($F_B \gg F_F$), so that the robot can easily push itself forwards but will not slip backwards when loaded with a draw rope.

Lin et al [27] produced a robot capable of AF using high-friction semi-rigid “ribbons”. To grip the pipe walls, the ribbons are pressed against the pipe walls and make contact across a large area, providing high friction. To release the pipe walls, the angle of the ribbons relative to the wall increases, sloping the ribbons away from the wall and decreasing the contact area, reducing the friction. Lin et al were able to achieve high AF of $f = 3.32$, but the constant bending could wear the ribbons, and the ribbons must be actuated into the correct position to achieve the correct grip/release state, increasing the complexity of the robot.

Rafsanjani et al [36] implemented AF through a kirigami skin modelled after snake skin. Kirigami skins are sheets of a material with patterned slits cut into the surface. When a coplanar force is applied to the skin, the patterned slits cause 3D features to pop up from the surface. The angle of the pop-ups provides high friction in one direction and low friction in the other. Rafsanjani et al were able to produce $f = 3.86$, although these were measurements recorded on a flat surface, not within a pipe - the surrounding walls of a pipe should provide more contact area, and thus more friction and a higher f . A weakness of the mechanism is that the robot body must be in contact with the pipe walls for the skin to provide the AF, making the robot fill the diameter of the pipe and making it hard to navigate around any obstructions. This method also requires

actuation to work (through the coplanar force), increasing the complexity of the robot.

Saab et al [33] used an “Anisotropic Friction Skin” (AFS) to implement AF that achieved a lower score of $f = 1.30$, however their implementation relies on the material properties of the AFS instead of a mechanical linkage. The specific material of the AFS is not disclosed, but the research presents the interesting idea of an inchworm AF mechanism that is completely passive, requiring no moving parts or complex mechanisms and potentially creating a lighter, smaller inchworm robot.

Bristle Assemblies

Similar to the AFS developed by Saab et al, “Bristle Assemblies” are passive components that provide anisotropic friction that could be used to create an inchworm robot. Bristle assemblies were originally designed and manufactured for “PipeBots” vibration robotics research [37]. Their construction consists of a cone-shaped arrangement of flexible rods, called “bristles”, that are uniformly distributed around in a circular pattern. The bristles are connected at the apex using a 3D printed clamp that provides an M2 screw mounting point for the bristle assembly. An example bristle assembly is shown in Figure 2.2.

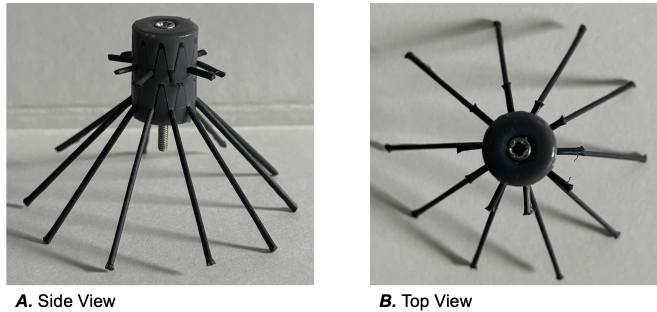


Figure 2.2: An example bristle assembly constructed from PVC bristles and “Tough 2000” [38] resin

A bristle assembly implements anisotropic friction as shown in Figure 2.3. When inserted into a pipe, the ends of the bristles make contact with the walls of the pipe. When pulled forward, the friction of the pipe wall on the bristles bends them backward, and the bristle assembly can slip forward. When pulled backwards, the bristles cannot bend, and as such, provide high friction, stopping the bristle assembly from moving. Unfortunately, no f value has been determined for the bristles, so experimentation is required to assess their performance.

The bristle assemblies require no moving parts to implement the GR mechanism and can be easily made from inexpensive materials (PVC). As such, they are an inexpensive and simple solution to anisotropic friction. They are easy to integrate into an assembly through the M2 mount. There is a large existing supply of pre-assembled bristle assemblies of various configurations of bristle material, thickness, and angle (as shown in Figure 2.4), allowing rapid testing of different bristle parameters to find the optimum bristle assembly.

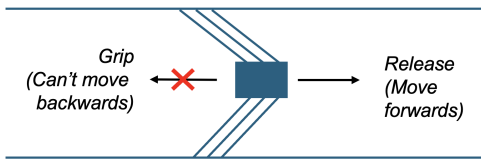


Figure 2.3: Bristle assembly providing the grip/release mechanism through anisotropic friction.



Figure 2.4: Existing bristle assemblies

A robot supported by bristle assemblies will be suspended in the middle of the pipe, allowing it to avoid colliding with any anomalies along the pipe walls, such as debris or other cables. Due to their compliant construction, the bristles should also bend around any anomalies they come into contact with, allowing a robot to traverse a non-empty pipe. If bristles get damaged or broken and no longer contact the pipe wall, the bristle assembly will have less grip on the pipe walls and the robot will potentially have a lower pulling force. Anisotropic friction also restricts the robot from travelling backwards; if the robot cannot move forward in a pipe, the only way to retrieve it is by manually pulling it out. This could break the bristles, but due to their low cost and easy construction, it is not deemed an issue in this project. Finally, as the bristles are constantly in contact with the walls of the pipe they are likely to wear due to the constant friction, meaning that bristle assemblies will have to be replaced over time.

Overall, although the f score of the various bristle assemblies requires experimental validation, they are a viable GR mechanism due to their small, simple construction and passive AF mechanism.

2.5 Cylindrical Cams

2.5.1 Principle of Operation

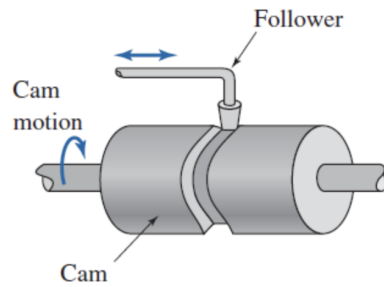


Figure 2.5: Cylindrical Cam [39]

As mentioned in subsubsection 2.4.2, cylindrical cams have high potential to create small, fast inchworm elongation and contraction mechanisms. A cylindrical cam con-

verts rotation into linear motion parallel to the axis of rotation, as illustrated in Figure 2.5. As the cam rotates, the follower moves backward and forward, following the groove of the cam path. This highlights the advantages of cylindrical cams over radial cams; radial cams produce reciprocation orthogonal to the axis of rotation, requiring bulkier mechanisms, whilst cylindrical cams keep the reciprocation along the original rotation axis, slimming down the mechanism and allowing for a smaller inchworm EC mechanism.

2.5.2 SVAJ Diagrams

To build an inchworm elongation and contraction mechanism, an engineer must be able to design how far and how fast the inchworm elongates and contracts. Cylindrical cams provide this ability through “SVAJ” (Speed, Velocity, Acceleration, Jerk) diagrams (illustrated in Figure 2.6): a graphical representation of the cam follower’s displacement over one revolution of the cam shaft, with follower displacement on the y-axis, and rotation on the x-axis.

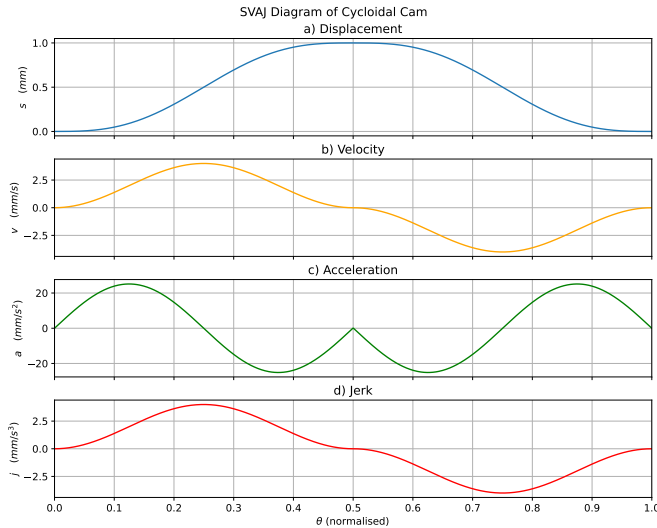


Figure 2.6: Cam SVAJ Diagram

From the displacement (aka, cam path), an engineer can calculate the first derivative, velocity, the second derivative, acceleration, and the third derivative, jerk, of the cam as shown in Figure 2.6. The “fundamental law of cam design” [34] states that the jerk function must be finite across a cam’s entire rotation to reduce impact, vibration, noise, and wear and tear. In an inchworm robot, harsh impacts and excessive vibration could damage the robot’s assembly, and thus SVAJ diagrams allow an engineer to design cam paths that minimise impact and vibration transmitted to the inchworm.

2.5.3 Rises, Dwells, and Returns

The phases of a cam’s motion can be categorised as follows [40]:

- **Rise** - the motion of the follower away from the initial position.

- **Dwell** - the motion during which the follower is at rest.
- **Return** - the motion of the follower towards the initial position.

Combining different phases of cam motion can be used to create different cam paths, as shown in Figure 2.7. In an EC mechanism, the Rise and Return phases can be used to elongate and contract the inchworm, whilst the Dwell phases will keep the robot stationary, allowing other mechanisms to actuate (e.g., a GR mechanism).

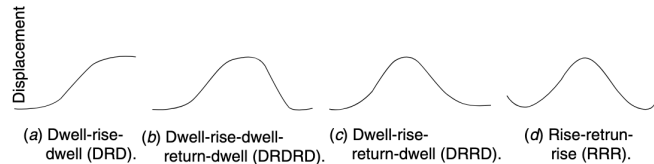


Figure 2.7: Examples of Cam Follower Motion, characterised with Rise, Dwell and Return phases [41].

2.6 Summary

The review first explained the need for faster, automated draw-rope laying in fibre optic cable ducts before covering some fast commercial pipe traversal robotics. The commercial solutions were too large for the fibre ducts, but they showcase impressive traversal speeds of up to 150 mm/s. The review then turns to inchworm robotics, as inchworm locomotion enables low-diameter robots. The elongate and contract mechanism is explored first: pneumatic inchworms are found to achieve fast speeds of up to 24 mm/s whilst remaining < 50 mm in diameter, but the external infrastructure required to power pneumatics is deemed too unwieldy, complex, and costly for the project. SMA springs are briefly contemplated as an actuation method due to their small size and ease of control, but are quickly disregarded due to their slow actuation speeds (2.5 mm/s) and fragile construction. Motor-based linkages are found to achieve speeds of up to 138 mm/s, but are uncommon in inchworm robotics due to the complexity and size of the mechanisms. 3D printing is identified as a solution to miniaturising these mechanisms.

For the wall gripping and releasing mechanism, anisotropic friction (AF) was introduced and explained, and existing anisotropic-friction-based inchworms analysed. Passive AF mechanisms with no moving parts are identified as an interesting solution due to their low assembly complexity and ease of integration - bristle assemblies are highlighted as a potential option.

Finally, the review explained the background knowledge and theory behind cylindrical cams in order to provide the reader with sufficient knowledge to understand the mechanisms involved in the project.

3 Cylindrical Cam Design

3.1 Introduction

The literature review identified cylindrical cams as a potential solution to the elongation/contraction (EC) (Figure 3.1) mechanism of an inchworm. This chapter explores the design of a miniature cylindrical cam using Python [42] and Autodesk Fusion [43], as well as the assembly and testing of a prototype cam to determine its usability in the EC mechanism of an inchworm.

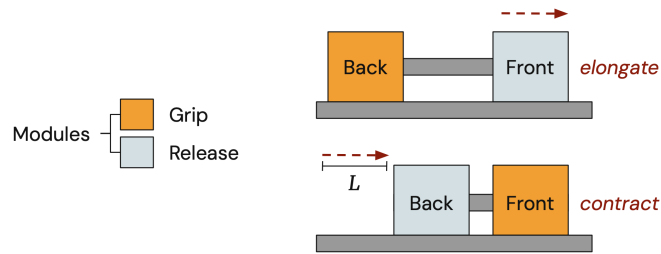


Figure 3.1: Elongate Contract mechanism.

3.2 Cylindrical Cam

As covered in section 2.5, cylindrical cams produce oscillatory linear motion when provided with an input rotation. The “motion path” of the cam follower’s output can be designed using SVAJ diagrams, allowing an engineer to design cams to meet displacement, velocity, acceleration, and jerk requirements. As cams are powered by continuous motor rotation in a single direction, high-speed motors can produce high-speed reciprocation in the cam follower. The motor also never has to change direction, so control is simple.

Cylindrical cams have their disadvantages. As the motion profile of the cam is defined by its physical geometry, the cam cannot be reprogrammed to follow a different motion profile, unlike most other linear actuators (e.g., lead screws). As such, cams must be manufactured for a specific purpose and are unlikely to be reusable across projects. If a new cam is needed, the old one must be discarded and a new cam manufactured, causing unnecessary waste and costing time and material.

3.3 Design

3.3.1 Cycloidal Curves

In inchworm locomotion, the elongation and contraction phases take the same amount of time. This means a symmetrical cam path was required, and as such, a DRDR (dwell-rise-dwell-return) cam path was chosen. The dwell phases allow the inchworm

to be temporarily stationary between elongation and contraction, allowing time for a grip/release mechanism to operate.

A cycloidal curve (also known as a “cycloid”) was chosen for the cam as it maintains continuous acceleration throughout one revolution, resulting in finite jerk [34], complying with the “fundamental law of cam design” mentioned in section 2.5. Cycloidal curves start and end with zero velocity, allowing dwell phases to be integrated at each end of the curve. One cycloid curve forms the rise of the cam, and another forms the return.

The SVAJ equations of the cycloidal curve can be found in Equation 3.1 [34]. θ is the normalised angle of the cam shaft, 0...1. β is the normalised angle at which the cycloid curve should reach its maxima. To produce a symmetrical cam, the curve must reach its maximum halfway through one rotation, before descending symmetrically back to 0. Thus, β is 0.5.

$$\begin{aligned} \theta &= \text{Cam angle of rotation} = 0\ldots1, \quad \beta = \text{Angle of Cycloid Curve Maxima}, \quad u(\theta) = \frac{\theta}{\beta} \\ \text{Displacement: } s(\theta) &= u(\theta) - \frac{\sin(2\pi \times u(\theta))}{2\pi} \\ \text{Velocity: } s(\theta)' &= v(\theta) = \frac{1}{\beta} (1 - \cos(2\pi \times u(\theta))) \\ \text{Acceleration: } s(\theta)'' &= a(\theta) = \frac{2\pi}{\beta^2} \sin(2\pi \times u(\theta)) \\ \text{Jerk: } s(\theta)''' &= j(\theta) = \frac{4\pi^2}{\beta^3} \cos(2\pi \times u(\theta)) \end{aligned} \tag{3.1}$$

The SVAJ equations can be mapped to an angular velocity ω as shown in Equation 3.2 [41]. These show that a linear increase in ω can produce an exponential increase in the acceleration of the cam, and thus (through $F = ma$) the force required to accelerate the cam. This has implications on the cam’s torque requirements, which will be covered in section 4.5.

$$\begin{aligned} t &= \text{Time (s) for cam to rotate through angle } \theta \\ \omega &= \text{Angular Velocity} = \theta/t \\ \text{Mapped Velocity } \dot{v} &= \omega v, \quad \text{Mapped Acceleration } \dot{a} = \omega^2 a, \quad \text{Mapped Jerk } \dot{j} = \omega^3 j \end{aligned} \tag{3.2}$$

3.3.2 Cam Path Generator

To model the cam, the cycloidal curve needed to be imported into the CAD software, Autodesk Fusion [43]. Unfortunately, Fusion has no native support for generating equation-driven curves (i.e. cycloids). Thus, a platform had to be built to enable generating Fusion-compatible curves using cycloidal equations. A Python [42] program named the “Cam Path Generator” was developed to bridge this gap. The script works as follows:

1. The user sets the desired cam follower stroke length and cam shaft radius.
2. The user runs the program, which generates a cycloidal cam path to match the

user's inputs.

3. The program saves the cam path as a “.csv” file.
4. The user imports the “.csv” file into Fusion using the open source “ImportSplineAnyCSV” Fusion plugin [44].
5. The cam path is imported into the Fusion project in the form of a spline curve, which can be integrated into a sketch.

The Cam Path Generator also produces an SVAJ plot of the cam shaft rotating at different angular velocities, shown in Figure 3.2, using the equations shown in Equation 3.2. The SVAJ plot is mapped onto the radius and stroke length L of the cam, allowing an engineer to predict the velocity, acceleration and jerk of the cam in use. The cam shown has a stroke length of 3mm and cam shaft radius 2.5mm and has SVAJ calculations for 200,400 and 600 RPM - the exponential increase in acceleration as RPM increases can be seen. These predictions are not exact - tolerances, manufacturing defects, and

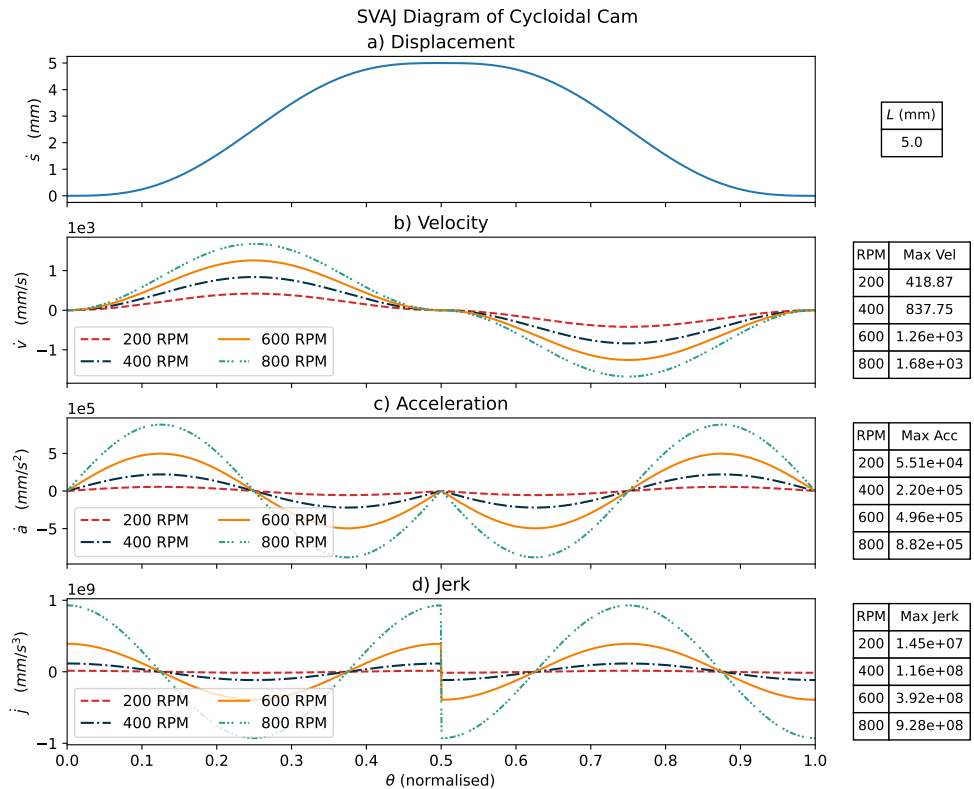


Figure 3.2: SVAJ plot generated by the Cam Path Generator

friction in the real cam will alter its displacement, affecting the SVAJ measurements. However, it is still a useful tool to estimate the cam's performance at different angular velocities. Source code for the Cam Path Generator can be found in Appendix F.

3.3.3 Fusion Design

Once generated, the cam “.csv” output can be used in Fusion as illustrated in Figure 3.3. In part A, the cycloidal curve is generated and exported to the “cycloid.cam.csv”

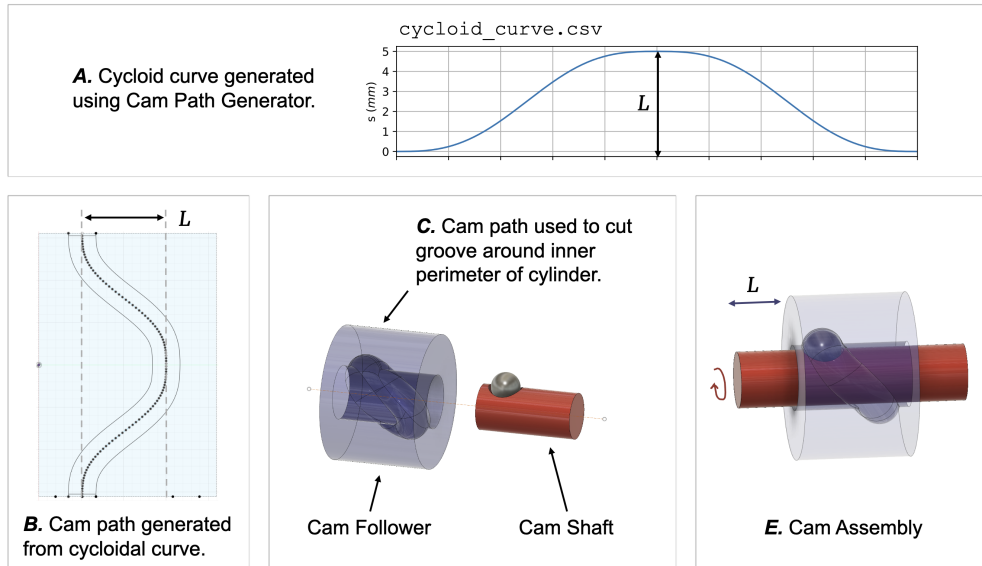


Figure 3.3: Designing a cam from the cycloidal curve

file, before being imported into the Fusion project. In part B, the curve is integrated into a sketch to create a profile of the cam groove. The cam path is then used in part C to cut a groove with a semi-circular profile into the inner circumference of a cylinder - this is the cam follower. A ball bearing of matching diameter fits within the groove with a small clearance, allowing it to roll around the groove. A semi-circular notch is also cut into the cam shaft, to constrain the ball bearing. Part E shows the final cam. By rotating the cam shaft, the ball bearing pushes against the cam groove and forces the cam follower into linear motion.

3.3.4 Reducing Moments

The aforementioned cam design has a flaw: the single point of contact between the cam and the follower (through the ball bearing) could introduce an unwanted moment on the cam shaft orthogonal to the axis of rotation. At high angular velocities this could push the cam shaft out of alignment and damage the assembly. To mitigate this, two identical cams were stacked along an axis, one rotated 180° , with their cam paths *in phase*, as shown in Figure 3.4. Ideally, the ball bearings will produce equal and opposite moments on the shaft that cancel each other out.

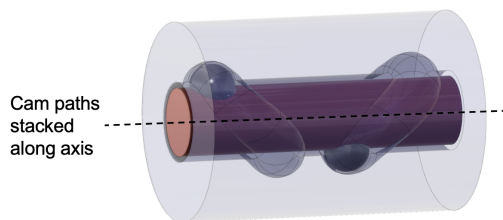


Figure 3.4: Two identical, in-phase cams stacked along the cam shaft axis and rotated 180° to cancel out their moments on the cam shaft.

3.3.5 Design for Manufacturability and Assembly

The cam was then redesigned with a “Design for Manufacturability and Assembly” [45] approach. This means that attention was given to how each part of the design would be manufactured and assembled, in order to:

1. Reduce the assembly time and complexity.
2. Reduce the number of parts.
3. Reduce the cost and time to manufacture.

The resulting cam design is shown in Figure 3.5. The cam was designed to be manufactured in two halves, as shown in part A. The loose ball bearings are inserted into one half and held in place with silicon grease, temporarily “sticking” the ball bearings to the cam. This allows the cam halves to be handled without the risk of the ball bearings falling out, and the silicon grease will function as lubricant once the cam is assembled.

The cam follower halves are aligned using alignment pins, as shown in part B. Correct orientation of each half is ensured by the ball bearings and cam grooves; an assembler won’t be able to close the cam in the wrong orientation.

The cam is then held together using press-fit locking rings, shown in part C. The locking rings remove the need for fasteners, increasing the ease of assembly and reducing the number of parts and tools required.

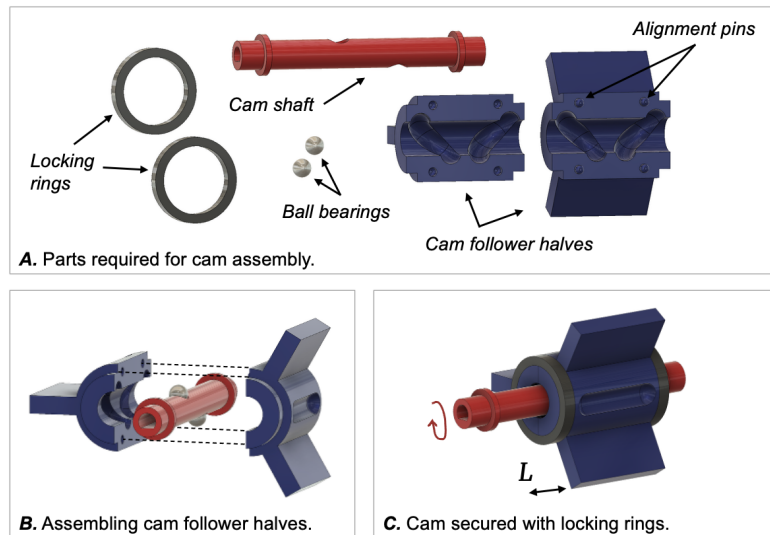


Figure 3.5: Cam assembly process

Protruding fins extend out of the cam follower to allow easy testing, as will be described in section 3.4.

3.3.6 3D Printing

The cam halves, cam shaft and locking rings were designed to be 3D printed to allow for fast prototyping. Alternative manufacturing methods such as injection moulding [46]

may be more suitable for manufacturing at volume, but may struggle to achieve the complex geometries of the cam path. The parts were printed using a “BambuLab X1-C” FDM printer [9] in PLA as it was readily available in the lab, and known to print well on the printer. Ideally, the cam would be manufactured from a material better suited for functional parts, such as ABS or PETG [47] to improve its longevity.

The cam was printed at a layer height of 0.08mm to allow for the smoothest possible finish on the cam paths, with the aim of reducing friction on the ball bearings. The printed cam parts can be seen in Figure 3.6 and the fully assembled cam can be seen in Figure 3.7.

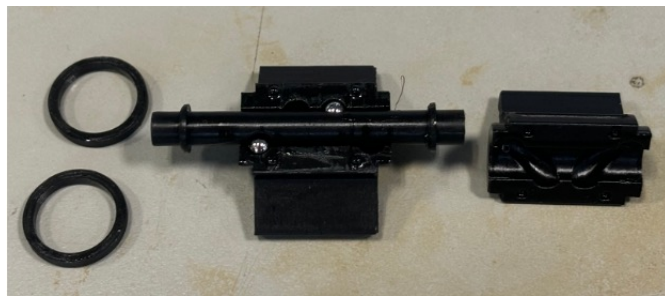


Figure 3.6: 3D printed cam parts and ball bearings, lubricated.

3.3.7 Tolerances

Ball Bearing Grooves

Seven tolerance values within a range of 0.1 to 0.7mm were tested for the ball bearing groove tolerances. The best fitting tolerance was 0.3mm, as this allowed the ball bearing to roll smoothly with minimal friction, although there remains a slight amount of radial and axial play between the shaft and the cam.

Locking Rings

The locking rings needed to be tightly fitted to the cam follower halves in order to hold them together, and the friction needed to be high enough to keep the rings attached during the cam’s high speed movement. 3D printing press-fit tolerances were researched (0.254mm to 0.4mm) [26] and tested, but the most optimal solution resulted from printing the rings with 0mm tolerances and lightly sanding down their inner circumference to produce the desired fit.

3.4 Testing

3.4.1 Velocity Tests

Once assembled, the cam was mounted in the chuck of a “18V XR Dewalt Drill Driver” [48] as shown in Figure 3.7. The cam follower was rotationally constrained using the protruding fins. The drill was engaged and the cam follower successfully reciprocated at the drill’s maximum speed of 1750 RPM [48]. The cam follower performs one elongation and one contraction of stroke length L per cam shaft rotation, allowing the average cam

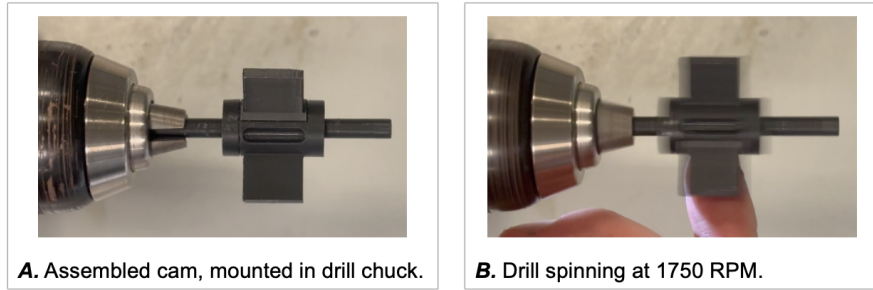


Figure 3.7: Cam mounted on Dewalt drill.

follower velocity in one direction to be calculated as shown in Equation 3.3.

$$1750 \text{ RPM} = 29.17 \text{ rev/sec}$$

$$29.17 \times L = 29.17 \times 3 \text{ mm} \quad (3.3)$$

$$\text{Average Velocity} = 183.3 \text{ mm/s}$$

At 1750 RPM the cam moves forwards around 183 mm/s, showcasing the cam's potential utility for producing a fast-moving inchworm robot.

3.4.2 Displacement Tests

At a slower speed, the cam shaft was rotated through 0° , 180° , and 360° , and the cam follower's displacement measured using digital calipers. The results, shown in Figure 3.8, show that the measured maximum displacement of 3.6 mm exceeded the desired stroke length L of 3 mm - this is likely due to the suboptimal tolerances of the cam grooves.

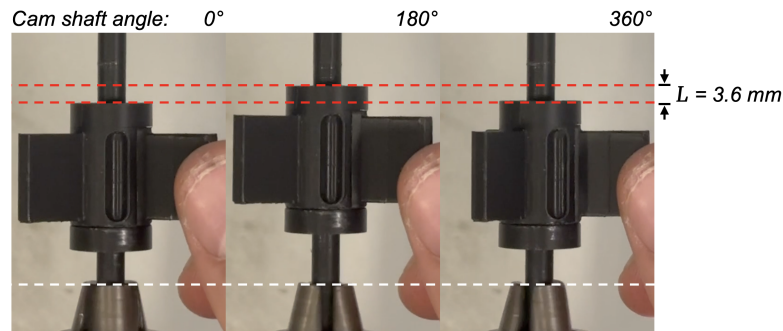


Figure 3.8: Measuring the cam stroke length L at different cam shaft angles.

3.5 Discussion

The Cam Path Generator successfully generated a cycloidal cam curve and outputted an SVAJ plot. The cycloidal curve cam contains two dwells, allowing the follower to be stationary between elongation and contraction and providing time for a grip/release mechanism to actuate. However, these dwell phases introduce large discontinuities in jerk as shown in the SVAJ plot (Figure 3.2) at $\theta = 0$ and 0.5 . These jerk discontinuities

increase exponentially with angular velocity and, at high speeds, can produce vibrations [34] that could have harmful effects on the cam assembly. By removing the dwell phases and implementing a rise-return (RR) cam path, the jerk would remain continuous, and less vibration would be induced at high speeds, creating a more robust cam. Two examples of effective RR cam curves are shown in Appendix D.

The Fusion workflow successfully integrates the cam curve into a 3D design, completing Objective 1. However, the workflow requires some manual input from the engineer to perform the CAD modelling, and could be improved by fully automating the CAD modelling stages. This could be achieved by developing a custom Fusion plugin [43] in Python that automatically performs the CAD modelling and outputs a pre-built cylindrical cam.

The Design for Manufacturing approach successfully created a design that requires minimal parts. However, the locking rings started to wear down after multiple attach/detach cycles. If the wear gets too significant the locking rings could detach during cam operation and the cam would fall apart, breaking the EC mechanism. The wear could be reduced by using more durable materials such as ABS or PETG, or the locking rings could be replaced with screws and threaded inserts, although this could likely increase the size of the cam assembly and thus the size of the robot.

The cam groove tolerance also remains suboptimal. During operation there is “play” in the cam follower, allowing it to tilt. To solve this, in future designs the cam shaft and follower are externally constrained by bearings, as will be seen in chapter 4. The suboptimal tolerance also allows for a stroke length of 3.6mm, larger than the intended 3mm. As the play is small (only 0.6mm) and unlikely to affect the successful operation of the robot, no actions are taken to fix it, although in the future, higher resolution manufacturing methods such as SLA printing could be used to manufacture a robot with higher resolution tolerances to remove the axial and radial play.

Overall, the produced cam was able to move the desired stroke length (3mm) and was able to operate at high speeds (1750RPM), successfully completing Objective 2. However, the 3mm stroke length is small and requires the cam shaft to rotate at very high speeds to achieve high cam follower speeds. Future iterations should have a larger stroke length to allow for equivalent cam follower speeds at lower RPMs, which will produce a faster inchworm robot.

4 Inchworm Prototype

4.1 Introduction

With the completion of objective 2, the cylindrical cam was ready to drive the elongation and contraction mechanism of an inchworm robot. This chapter details the design and construction of the inchworm robot, as well as design optimisations performed to increase the speed of the inchworm robot. Bristle assemblies were selected for the prototype's GR mechanism due to their availability, low-cost construction, and ease of integration.

4.2 Inchworm Chassis

The inchworm chassis was designed using Fusion. The chassis connects the cylindrical cam to a motor and the cam follower to the front bristle assembly, as shown in Figure 4.1. Threaded inserts were added to the front and back of the chassis to allow for easy mounting of the bristle assemblies. The front attachment (**B**) is a separate part that attaches to the cam follower with a pin.

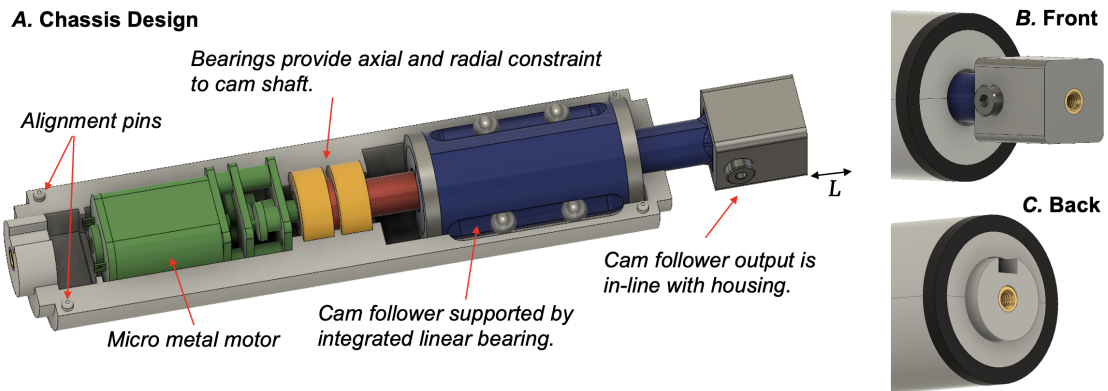


Figure 4.1: (A) Inchworm prototype design. (B, C) Threaded inserts for bristle attachments.

Like the cam, the chassis was designed in two halves that are aligned with alignment pins and secured together using locking rings, as indicated in Figure 4.2. The cam shaft is radially and axially constrained by two deep groove ball bearings. The cam follower is constrained by a linear bearing integrated into the design, explained in subsection 4.2.1. The cam shaft couples to the motor through a D shaft and a matching slot. For testing purposes, a 420RPM "Micro Metal" motor [49] was selected. Micro Metal motors are available in various gear ratios, but all have the same physical dimensions, allowing testing of multiple gear ratios as explored later in section 4.5. The ball bearings and motor are fully constrained by cutouts on each side of the chassis, and the stroke length L has been increased to 5mm to enable faster cam follower movement and thus produce a faster inchworm.

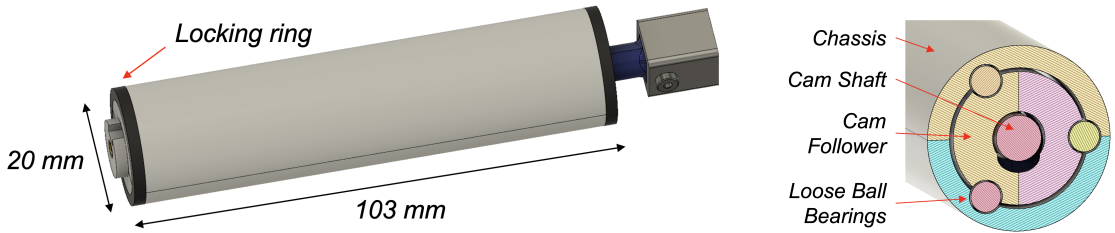


Figure 4.2: Closed inchworm robot, secured with locking rings.

Figure 4.3: Cross section of integrated linear bearing.

4.2.1 Integrated Linear Bearing

The integrated linear bearing allows the cam follower to oscillate axially whilst remaining rotationally and radially constrained. It works by suspending the cam follower between 3 circumferentially distributed tracks containing loose ball bearings, as shown in Figure 4.3. Integrating the linear bearing into the chassis reduces the size of the inchworm robot, the ball bearing grooves can fit around existing features, and room doesn't have to be made for integrating separate parts. The linear bearing concept was tested as a sub-assembly using the same approach described in section 3.4; the assembly operated successfully at 1750 RPM (Appendix A).

4.2.2 Assembly

The inchworm chassis was 3D printed in PLA and assembled (Figure B.1). A power tether was soldered to the motor, and silicon grease applied to the cam mechanism to reduce friction. An arbitrary bristle assembly was chosen, labelled bristle assembly A, and attached as shown in Figure 4.4, forming the first functional prototype of the inchworm robot. Unfortunately, the non-ideal ball bearing tolerances of the linear bearing



Figure 4.4: First functional prototype of the inchworm, integrating the motor, cylindrical cam, and bristle assemblies.

created axial play in the cam follower output, potentially producing friction in the output reciprocation and lowering the cam follower velocity. The locking rings are also prone to wear as described in section 3.5.

4.3 Initial Velocity Tests

4.3.1 Setup

Once assembled, the inchworm prototype was tested to assess its velocity as a draw rope laying robot. The robot was inserted into a pipe of 50 mm internal diameter and

978 mm length, matching the diameter of the Openreach fibre optic cable ducts. The power tether was supplied with 6V from a desktop power supply unit, with a current limit set to the motor's stall torque [49] to protect the motor. The power tether also emulates the draw rope, as the robot must tow the power tether behind itself as it moves. A camera was set up to record footage of the inchworm's progress.

4.3.2 Methodology and Results

The power supply was activated and the time it took the robot to reach the end of the pipe was measured using a stopwatch. The experiment was repeated five times and the average time calculated. A limitation of this method is its precision; user error in stopwatch timing could affect the resulting velocity calculations, so future tests could utilise time-of-flight sensors to record the displacement of the robot. A recorded segment of the robot's journey can be seen in Figure 4.5. The robot travelled 978 mm in an average of 80 seconds, and thus achieved an average velocity of 12.23 mm/s.

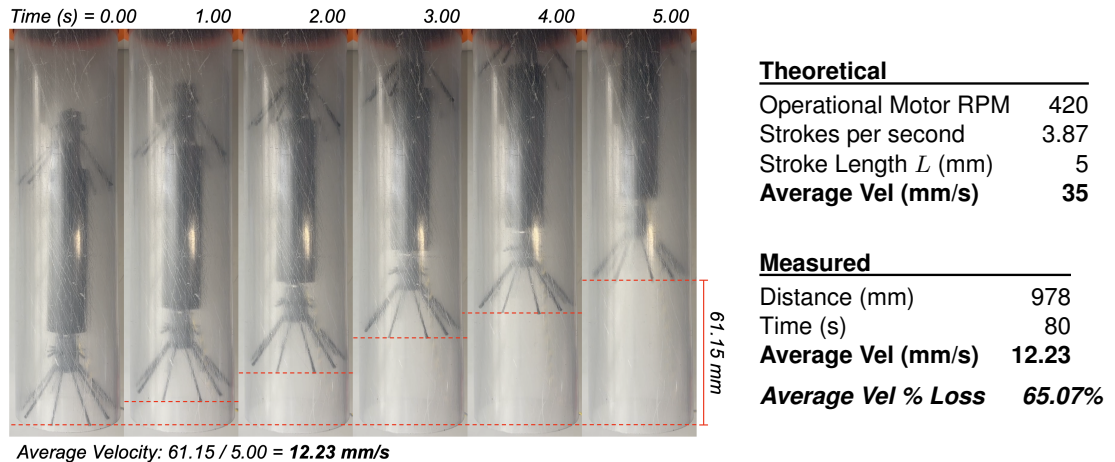


Figure 4.5: Footage of inchworm velocity test, as well as theoretical vs measured inchworm velocities.

4.3.3 Analysis

The theoretical velocity of the inchworm robot can be calculated from the RPM of the motor (from section 4.5) and the stroke length L of the robot, as shown in Figure 4.5. Assuming the robot travels L mm per motor revolution, and the motor revolves 3.86 times per second, the robot should be travelling at $3.86 \times 5 = 19.33$ mm/s. The robot was actually travelling at 12.23 mm/s, meaning the prototype was suffering a 65.07% loss in velocity.

The experiment footage was analysed frame by frame, and it was discovered that during the elongation phase of movement, the bristles were slipping backwards against the walls of the pipe - i.e. the bristles did not provide enough friction in the backwards direction to sufficiently anchor the back of the inchworm. This is illustrated in Figure C.1. Thus, it became clear that higher friction bristles were required for the grip phase of the GR mechanism. It is also unlikely the motor was running at its maximum RPM of 420

RPM due to the torque load. As such, the motor's operational RPM was investigated, as explained in section 4.5.

4.4 Bristle Assembly Friction Coefficients

4.4.1 Bristle Friction

To fix the slipping bristles, an experiment was conducted to assess the static friction coefficients of each direction of various bristle assemblies. The forward (release) friction F_F of a bristle assembly must be low enough to be overcome by the elongate/contract mechanism, whilst the backwards (grip) F_B friction must be high enough to provide the robot with a strong enough pulling force to pull a draw rope without the bristles slipping. Thus, the optimal bristle assembly will have the highest value of $f = F_B/F_F$.

4.4.2 Setup

An experiment to measure F_F and F_B for each of the pre-existing bristle assemblies was performed as follows. A test rig was designed to suspend a single bristle assembly in the center of the 50mm ID pipe. The bristle assembly attaches to a "slider" via an M2 screw and threaded insert, shown in Figure 4.6. The slider slides into a "mount" that press-fits on to the end of the pipe and holds the bristle assembly in the middle of the pipe. The slider slides in and out of the mount with negligible friction.

4.4.3 Methodology

To measure F_B a bristle assembly was attached to the slider, facing backwards. A newton meter was used to apply a pulling force to the bristle assembly through the slider, as shown in Figure 4.6. The force slowly increased until the bristle assembly slipped backwards, at which point the force was recorded. A camera was used to track the exact force value at which the bristles slipped. To measure F_F the bristle assembly was attached in the reverse direction to pull it forward out the pipe. Once the friction coefficients of a bristle assembly were found, two matching assemblies were attached to the inchworm and the velocity experiment from section 4.3 was repeated to measure the effective velocity of the assembly.



Figure 4.6: Newton meter measuring the F_B coefficient of a bristle assembly

4.4.4 Limitations

The original plan was to use a Mecmesin [50] tensile tester to apply the pulling force and precisely measure the slipping forces, however the equipment in the lab was out of service. As the Newton metres are not as accurate as the tensile tester, various measures were taken to ensure accurate readings: newton meters of increasing ranges were used to allow for higher-precision measurements, and each measurement was repeated five times and averaged to compensate for any inaccurate readings.

4.4.5 Results

Originally, all available bristle assemblies were going to be measured. However it soon became clear that bristle assemblies with feet (deposits of material at the end of the bristle to aid friction on the pipe wall) performed much better than non-footed bristles. As such, the remaining non-footed bristles were abandoned.

The specifications and results of the bristle assemblies selected for testing are shown in Table 4.1 and the results plotted in Figure 4.7. All bristles had a diameter of 1 mm. The green dashed horizontal line is the ideal velocity of the inchworm based on calculations from section 4.3 (35 mm/s). The vertical grey dot-dashed line is the minimum force exerted on the bristle assemblies during the elongation phase of movement, based on the force required to accelerate the average mass of a bristle assembly at the ideal motor RPM, as shown in Equation 4.1.

$$\omega_{\text{ideal}} = \text{Ideal Motor RPM} = 420, \quad m = \text{Average Bristle Assembly Weight} = 8.77g, \quad L = 5\text{mm}$$

$$a = \text{Cam Follower Acceleration} = \frac{\omega_{\text{ideal}}}{60} \times L = \frac{420}{60} \times 5 = 35\text{mm/s}^2$$

$$F_{\min} = ma = 8.77 \times 10^{-3} \times 35 = 0.30N$$

(4.1)

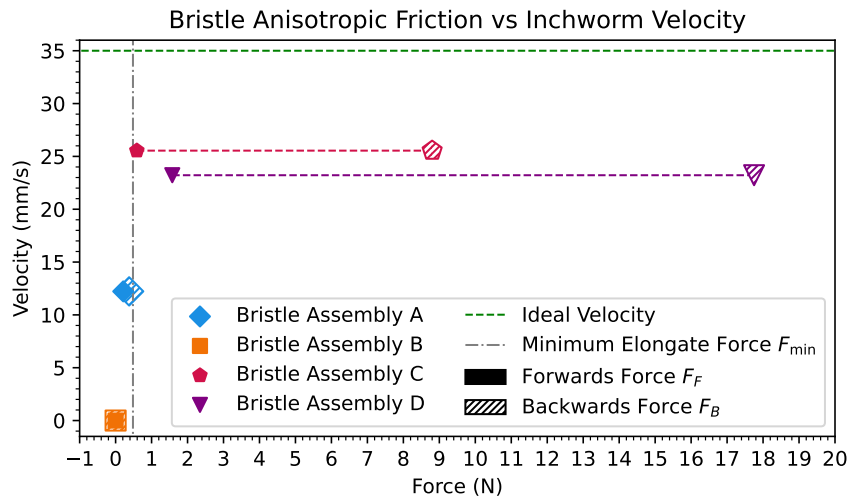


Figure 4.7: Measurements of static friction coefficients of various bristle assemblies



Figure 4.8: Inchworm with Assembly C

Table 4.1: Construction and performance of different bristle assemblies.

Assembly	Construction			Performance			
	Foot	Bristle	Angle ($^{\circ}$)	F_F (N)	F_B (N)	f	Vel (mm/s)
A	-	PVC	65	0.21	0.38	1.81	12.20
B	-	PETG	65	0	0	0	0.00
C	PX30 Resin [51]	PVC	25	0.59	8.80	14.90	25.50
D	PX30 Resin	Steel	25	1.58	17.75	11.23	23.20

4.4.6 Analysis

The bristle assembly tested in section 4.3 was bristle assembly A. Footed bristles (C, D) have high values of f and high velocities. Non-footed bristles (A, B) have low values of f and low velocities. The results show that footed bristles provide a much higher F_B , whilst maintaining similar values to non-footed bristles for F_F . The proximity of F_{\min} to bristle assembly A F_B explains the slipping behaviour observed in the initial velocity experiment. F_{\min} was overpowering F_B , pushing the bristles backwards and forcing them to slip. However, due to the f value of 1.81, the backwards bristles still provided more friction than the front bristles, so the inchworm managed to move forward. Bristle assembly B made no progress due to the zero anisotropic friction difference ($f = 0$).

Bristle assembly C had the highest f value and produced the fastest inchworm robot at 25.5 mm/s, making it the optimum bristle assembly (shown attached to the robot in Figure 4.8). However, it is still 27% slower than the ideal value of 35 mm/s, indicating that further optimisations can be performed to increase the speed of the robot. Bristle assembly D was slower than C due to the higher F_F , but provides a gripping force F_B twice as strong due to the steel bristles having a higher stiffness than the PVC. Therefore, if the inchworm robot is required to pull a load that bristle assembly C can't handle, bristle assembly D should be used instead.

4.5 Motor Selection

4.5.1 Torque Profiles

The bristle selection experiment highlighted that 27% of the inchworm velocity was still being lost, even with optimal bristles; this was due to the non-ideal behaviour of the Micro Metal motor. Micro metal motors have torque-speed profiles that describe how their operating RPM changes depending on the torque load [49]. By comparing these torque-speed profiles against the average operating torque requirements of the cam across a range of RPMs, the actual operating RPM of the motor can be estimated, and by extension, the motor that drives the cam at the highest RPM can be selected.

4.5.2 Cam Torque

First, the torque requirements of the cam needed to be calculated. The front module of the robot is light; driving it forwards with the cam during elongation requires minimal

force, and thus minimal torque. The back of the robot is heavier as it houses the motor; pulling it forward (during contraction) requires more torque. The total force load on the cam during one cam revolution, F_{cam} , is shown in Equation 4.2. The cam follower acceleration $a(\theta)$ is obtained from the SVAJ diagrams shown in Figure 3.2.

$$\begin{aligned} \theta &= 0 \dots 1, \quad F_F = \text{Bristle forward force (N)}, \quad a(\theta) = \text{Acceleration of cam follower at } \theta (\text{mm/s}^2), \\ m_F &= \text{Front mass (g)}, \quad m_B = \text{Back mass (g)}, \quad F_{\text{cam}}(\theta) = \text{Force required to move the cam follower (N)} \\ F_{\text{cam}}(\theta) &= ma(\theta) + F_F, \quad m = \begin{cases} m_F & \theta \leq 0.5 \\ m_B & \theta > 0.5 \end{cases} \end{aligned} \quad (4.2)$$

The torque requirements of the cam can be calculated as a function of ω and θ using the torque equations derived by Rothbart [41] described in Equation 4.3.

$$\begin{aligned} \tau &= \text{Torque (Nm)}, \quad v(\theta) = \text{Cam follower velocity at } \theta (\text{m/s}), \quad \omega = \text{Cam shaft angular velocity (rad/s)} \\ \tau(\theta) &= F_{\text{cam}}(\theta) \times \frac{v(\theta)}{\omega} \end{aligned} \quad (4.3)$$

Figure 4.9 shows the torque calculation results across a range of ω as a function of θ using bristle assembly C, and specifies the maximum torque requirements of the cam at each RPM. The plot highlights the effect of the mass imbalance between the front and back modules; the cam requires the most torque when it contracts and accelerates the back module of the inchworm forwards at $\theta = 0.68$, due to the weight of the motor. In the future, additional features and components should be added to the front of the robot to balance out the torque response of the motor.

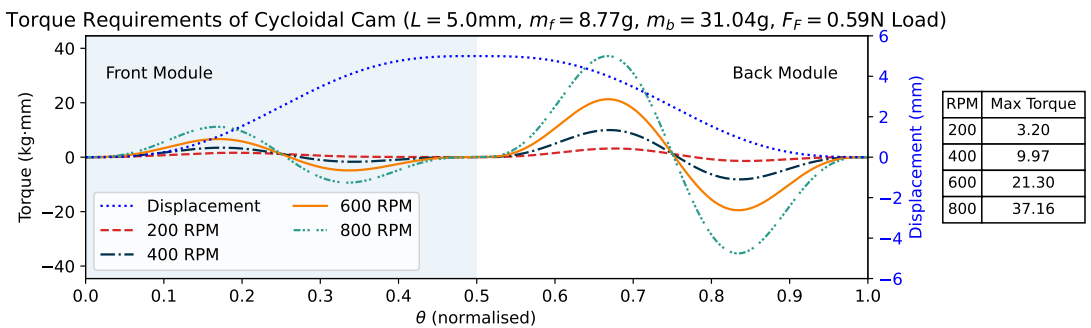


Figure 4.9: Cam torque plot generated by Cam Path Generator

4.5.3 Motor Torque

The inchworm's driving motor must be able to provide enough torque to drive the cam at its maximum torque. Ideally, the motor must also have a high RPM at the cam's average torque requirements in order to produce a fast robot. The average and maximum required cam torque can be plotted as a function of ω , as shown by the dashed lines in Figure 4.10. By plotting a selection of Micro Metal motor torque-speed profiles on the same axes, the operating RPMs of the motors can be found. The table shows

the numerical values of maximum and average operating torques required to drive the cam, as well as the average operating RPM, allowing an engineer to select a motor that will drive the cam at a high RPM without exceeding its stall torque. The figure also displays the theoretical velocity the inchworm robot should achieve using each motor calculated from the average RPM and stroke length L .

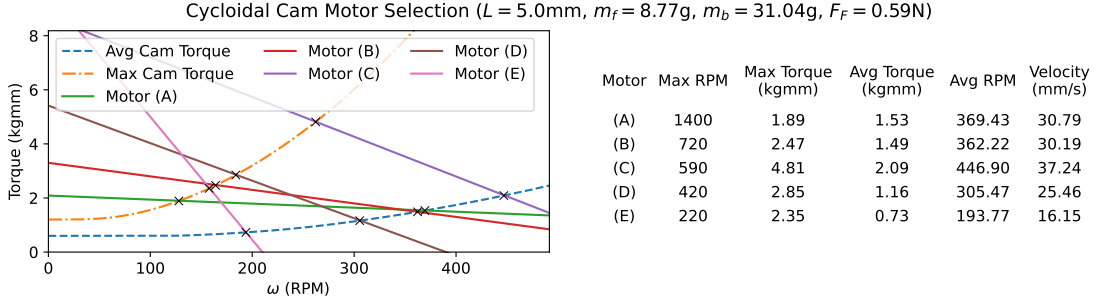


Figure 4.10: Torque profiles of various motors vs the cycloidal cam. The optimal motor can be seen to be motor (D), as it provides the highest average operating RPM.

So far, the inchworm has been using motor D. The plot shows that due to the torque requirements of the cam, the motor was operating at an average of 305 RPM, as opposed to the expected 420 RPM, giving a 27% velocity loss. Recalculating the ideal velocity with 305 RPM gives a value of $(305/60) \times 5 \approx 25 \text{ mm/s}$, much closer to the measured value of 25.5 mm/s.

The plot presents options for optimising the inchworm's velocity. Motor C provides the highest operating speed of 447 RPM for the inchworm. The maximum required torque at 447 RPM is 4.81 kgmm, which is less than the motor's maximum operating torque of 8.6 kgmm [49]. Thus, motor C is the optimum motor and should drive the inchworm at a speed of $(447/60) \times L = (447/60) \times 5 \approx 37 \text{ mm/s}$. Unfortunately, there was not enough time to source and test motor C, so future work is necessary to obtain the experimental velocity produced by the motor.

An experiment was designed to experimentally measure the torque requirements of motor D by logging its current consumption during inchworm locomotion and calculating its torque output using its torque-current profile [49]. The experiment was performed using an RSDM3055 Bench Digital Multimeter [52], but the sampling rate of the multimeter was too low to capture the current fluctuations within one full motor revolution, and thus, the torque fluctuations during a revolution could not be determined. The experiment should be repeated with a meter with a higher sampling rate to gather more precise data. A flaw in the approach is that it relies on the accuracy of the motor vendor's torque-current plot; as the motor heats up, the motor current consumption will increase, skewing the results.

4.6 Real World Testing - BT Adastral

With the inchworm robot tested and optimised, its capabilities could be tested in a real world environment. "BT Adastral" [2] provide accurate testing environments for cable duct robotics, as shown in Figure 4.11, using cable ducts taken from the field. The aim of the test was to assess the usability of the inchworm in a real world scenario. Thus, the test objectives for the inchworm were as follows: 1) traverse a total of 6 meters, 2) traverse a spigot and socket joint connecting two pipes, and 3) tow a draw rope the length of the pipe.

4.6.1 Setup

A 6 meter power tether was constructed for the test and connected to a 6V power supply. The inchworm was inserted into the start of the testbed duct. On-site researchers provided high-strength fishing line to use as draw rope for the test, however, the draw rope had a much lower mass than the power tether and thus was deemed unnecessary - if the robot was able to pull the power tether, it would certainly be able to pull the draw rope. The inchworm was equipped with motor D and bristle assembly C.



Figure 4.11: BT OpenReach fibre optic cable duct testbed, featuring two 3m x 50mm ID cable ducts connected by a spigot and socket joint.



Figure 4.12: Inchworm prototype stuck in the spigot and socket pipe joint

4.6.2 Methodology and Results

The power supply was engaged, and a stopwatch was used to record the time it took the robot to traverse the testbed. The robot successfully traversed the first 3-meter section of duct. However, once the robot reached the spigot and socket joint it was unable to progress due to the diameter of the joint being larger than the diameter of the bristle assemblies. The forward bristles were unable to grip the pipe, and thus the robot became stuck as shown in Figure 4.12. The robot was manually removed and inserted into the next section of pipe, where it successfully traversed the next 3-meter section. The average speed of the robot (over a 3m section) was recorded to be 16.67 mm/s.

4.6.3 Analysis

The robot successfully traversed 6 meters of pipe and dragged the power tether the whole distance, completing test objectives 1 and 3. However, the robot was not able to traverse the pipe joint due to the larger diameter. The solution to this would be to increase the length of the bristles, so that at larger diameters they spring out and make contact with the pipe walls, continuing their movement as before. The average speed measured in the test (16.67 mm/s) was much lower than the velocity recorded in the lab (25.50 mm/s). The 6 meters of power tether had a mass of 14.48 grams and will have produced friction with the pipe walls, slowing down the robot. The voltage drop across the power tether was also not taken into account, meaning that although the power supply was outputting 6V the motor would've received less, and thus would not be running at its optimum voltage.

4.7 Discussion

An inchworm prototype was successfully designed, manufactured, and tested. The chassis utilised Micro Metal motors to allow for testing of various gear ratios to find the optimal motor. Radial play in the chassis-integrated linear bearing could be introducing friction in the mechanism, decreasing the robot's speed. The initial version of the robot (using bristle assembly A) successfully performed inchworm locomotion but was slow (12.23 mm/s) due to slipping bristles - experimentation found that footed bristles mitigated the slipping issues and doubled the speed of the robot (25.5 mm/s). However, there were only two footed bristle options available for testing, so future work is required to further explore materials for footed bristles to increase their f value, and thus the inchworm's velocity.

Through analysing the theoretical torque requirements of the cam the original motor (motor D) was theorised to be operating at a lower angular velocity than expected. The analysis identified that motor C would operate the inchworm at a higher RPM, achieving a theoretical inchworm velocity of 37.24 mm/s, although experimental testing is required to validate the estimation.

The prototype performed less effectively in a real world test environment due to the resistance and friction of the power tether; future versions of the inchworm should carry their own power source to remove the need for a tether. Whilst this will make the robot heavier, and thus slower, it should allow it to travel further as its range will no longer be limited by tether length. By integrating a battery into the front inchworm module, the front and back module will be balanced and the maximum torque requirements of the cam shouldn't increase, as long as the battery is not heavier than the motor.

Overall, this chapter has achieved objectives 3 and 4 by creating a functional inchworm robot that is able to navigate fibre optic cable duct. Unfortunately the robot is not able to navigate spigot and socket joints used in the field due to the large diameter of the joints - longer bristles should solve this problem, but require experimental validation.

5 Conclusion

5.1 Achievements

1. Cam Path Generator Python Program

Developed a Python program to generate cylindrical cam paths from arbitrary curves, display SVAJ plots at different angular velocities, and export each cam path in a Fusion-compatible format, thus completing objective 1.

2. Miniature Cycloidal Cylindrical Cam

Produced a 3D-printed miniature cycloidal cylindrical cam, achieving objective 2.

3. Prototype Inchworm Robot

Produced a functioning inchworm robot that utilises cylindrical cams and anisotropic friction for propulsion, achieving objective 3.

4. Optimisation

Optimised the bristle assemblies and motor selection to produce a faster inchworm robot, achieving objective 4.

5.2 Discussions

The cylindrical cam workflow successfully enables the rapid design and prototyping of cylindrical cams based on curve equations. The SVAJ plots generated provided useful analysis on the force and torque requirements of the cam, enabling the selection of an optimal motor. The cycloidal cylindrical cam developed using the aforementioned workflow successfully operated at 1750 RPM, producing an average forward velocity of 183.3 mm/s across a 3 mm stroke length, proving the mechanism's functionality. A flaw of the mechanism is that cylindrical cams are not as general purpose as other linear actuators like lead screws. The cam motion path cannot be reprogrammed, so cams must be built for specific purposes and are unlikely to be reusable.

The cycloidal cam path provides dwell phases to allow the inchworm to be stationary during the GR phase of its locomotion, allowing a potential GR mechanism time to actuate. However, the anisotropic friction GR mechanism requires no actuation, and thus the dwell phases are not necessary. A rise-return (RR) cam path such as Sine Squared (see Appendix D) could enable a faster inchworm due to the lower acceleration requirements, requiring less torque and thus allowing the motor to operate at a higher RPM.

The bristle assembly test rig enabled the quantification of static friction coefficients and f scores of PipeBots Bristle Assemblies, allowing the optimisation of inchworms for either velocity or wall-grip force. The bristle assembly optimisation was used to produce an optimised inchworm capable of a maximum experimental velocity of 25.5

mm/s, and able to pull 6 meters of draw rope (14.5g) through a fibre duct. However, the robot was not able to traverse spigot and socket pipe joints - further experimentation on bristle length could solve this problem by increasing the reachable diameter of the bristle assemblies. The maximum pulling force of the robot is also unknown. A load cell could be used to record the pulling force of the robot and determine the optimal combination of bristle assemblies and cam paths for pulling force optimisations.

The cam-based inchworm performs well against other robots in the literature, achieving the highest maximum velocity of all the reviewed inchworm robots of < 50 mm diameter, as shown in Table E.1. The inchworm doesn't require the supporting infrastructure of pneumatic solutions, and is stronger and more robust than the SMA solution. However, the robot is much slower than the wheeled and tracked commercial solutions, indicating that inchworm locomotion is not ready to replace more traditional locomotion mechanisms.

Micro Metal motors were chosen to drive the inchworm due to their small dimensions and the range of gear ratios available. However, the motor speeds available were low (maximum 4400 RPM) and torque-speed profiles were poor; experimenting with motors with higher speeds and stronger torque-speed profiles could produce faster inchworm locomotion, but could increase the wear of the bristles.

5.3 Conclusions

This project developed a software workflow for generating cylindrical cams and produced an inchworm robot that utilises cylindrical cams and anisotropic friction for locomotion through 50 mm internal diameter pipes. The robot reached a maximum speed of 25.5 mm/s and was able to pull a 14.5g load, although further testing remains to quantify the maximum load of the robot. The robot was tested in a real-world fibre optic cable duct and successfully navigated straight sections, but was unable to navigate the spigot and socket joints.

5.4 Future Work

Future work would entail experimenting with larger diameter bristle assemblies to enable the robot to traverse socket and spigot joints. Then, integrating a power supply into the robot (i.e. batteries) would remove the need for a power tether, and the robot can be retested in the real world pipe ducts to assess its range and runtime. Further work could entail integrating two followers onto the same input cam shaft with 180° phase difference. These cams would move away from each other during the elongation phase leading to a combined stroke length of $2 \times L$, doubling the ideal velocity of the inchworm robot but also increasing the torque requirements of the motor.

References

- [1] R. Chataut, *Undersea cables are the unseen backbone of the global internet*, en-GB, Apr. 2024. [Online]. Available: <http://theconversation.com/undersea-cables-are-the-unseen-backbone-of-the-global-internet-226300> (visited on 08/01/2025).
- [2] BT, *Openreach*. [Online]. Available: <https://www.openreach.com>.
- [3] P. Digital, *Why choose us for draw cord? - RopesDirect*, en, Jan. 2023. [Online]. Available: <https://www.ropestdirect.co.uk/blog/why-choose-us-for-draw-cord/> (visited on 08/02/2025).
- [4] dagallagher@tscsubsea.com, *TRITON: Tethered In-line Inspection (ILI) Pipe Crawler*, en-US, Feb. 2024. [Online]. Available: <https://www.tscsubsea.com/introducing-triton-tethered-ili-pipe-crawler/> (visited on 07/08/2025).
- [5] Eddyfi Technologies, *Inuktun versatrax*.
- [6] *In Pipe Robotics — Our Products — Synthotech*, en-US. [Online]. Available: <https://synthotech.com/product-category/in-pipe-robotics/> (visited on 07/08/2025).
- [7] S. Kazeminasab, N. Sadeghi, V. Janfaza, M. Razavi, S. Ziyadidegan, and M. K. Banks, “Localization, Mapping, Navigation, and Inspection Methods in In-Pipe Robots: A Review,” en, *IEEE Access*, vol. 9, pp. 162 035–162 058, 2021.
- [8] Y. Peng, H. Nabae, Y. Funabora, and K. Suzumori, “Controlling a peristaltic robot inspired by inchworms,” en, *Biomimetic Intelligence and Robotics*, vol. 4, no. 1, p. 100 146, Mar. 2024, Publisher: Elsevier BV.
- [9] *Bambu Lab X1C — Carbon Fiber 3D Printer*, en. [Online]. Available: <https://uk.store.bambulab.com/products/x1-carbon> (visited on 07/01/2025).
- [10] SCREWFIX, *Screwfix draw rope*. [Online]. Available: <https://www.screwfix.com/c/electrical-lighting/fish-tape/cat6070004>.
- [11] Jetting, *V3 Fiber Blowing Machine*, en-GB. [Online]. Available: <https://jetting.se/v3/> (visited on 07/08/2025).
- [12] Power and Cables, *Cable Blowing Machines - FTTH FTTP Fibre Optic Cable Blowers*, en. [Online]. Available: <https://www.powerandcables.com/product/cable-pulling-laying/cable-blowing-machines/> (visited on 07/08/2025).
- [13] Cabling Installation & Maintenance, *Vacuum cleaner helps pull cable*, en, Dec. 1997. [Online]. Available: <https://www.cablinginstall.com/home/article/16467951/vacuum-cleaner-helps-pull-cable> (visited on 07/01/2025).
- [14] Trenchless Equipment, *What Do I Need To Know About a Duct Rodder? - Trenchless Equipment*, en-US, Apr. 2022. [Online]. Available: <https://trenchlessequipment.com/what-do-i-need-to-know-about-a-duct-rodder/> (visited on 07/08/2025).
- [15] Briticom, *Cable Rod - Duct Rodder*, en-GB. [Online]. Available: <https://briticom.net/product/cable-rod/> (visited on 07/08/2025).
- [16] Fremco, *Introducing DuctRod RAPID - the versatile duct rodder from Fremco*, en-GB, Apr. 2022. [Online]. Available: <https://fremco.dk/introducing-ductrod-rapid/> (visited on 07/08/2025).
- [17] J. Tan, Y. Yang, Z. Fan, Y. Wang, Q. Zhou, and Z. Wang, “Overview of Pipeline Inspection Robots,” en, *Academic Journal of Science and Technology*, vol. 9, no. 1, pp. 208–211, Jan. 2024.

- [18] E. Dertien and S. Stramigioli, "Basic maneuvers for an inspection robot for small diameter gas distribution mains," en, in *2011 IEEE International Conference on Robotics and Automation*, Shanghai, China: IEEE, May 2011, pp. 3447–3448.
- [19] J. Park, T. Luong, and H. Moon, "Development of a Wheel-Type In-Pipe Robot Using Continuously Variable Transmission Mechanisms for Pipeline Inspection," en, *Biomimetics*, vol. 9, no. 2, p. 113, Feb. 2024.
- [20] A. Kakogawa, K. Murata, and S. Ma, "Automatic T-Branch Travel of an Articulated Wheeled In-Pipe Inspection Robot Using Joint Angle Response to Environmental Changes," *IEEE Transactions on Industrial Electronics*, vol. 70, no. 7, pp. 7041–7050, Jul. 2023.
- [21] W. Wang, J.-Y. Lee, H. Rodrigue, S.-H. Song, W.-S. Chu, and S.-H. Ahn, "Locomotion of inchworm-inspired robot made of smart soft composite (SSC)," *Bioinspiration & Biomimetics*, vol. 9, p. 046 006, Oct. 2014.
- [22] D. Fang, J. Shang, Z. Luo, P. Lv, and G. Wu, "Development of a novel self-locking mechanism for continuous propulsion inchworm in-pipe robot," en, *Advances in Mechanical Engineering*, vol. 10, no. 1, p. 1 687 814 017 749 402, Jan. 2018.
- [23] Y. Di, Y. Zhang, Y. Wen, et al., "Inchworm-Inspired Bipedal Crawling Soft Robot With Forward and Backward Locomotion for Confined Spaces," *IEEE Robotics and Automation Letters*, vol. 10, no. 6, pp. 5839–5846, Jun. 2025.
- [24] K. Miyasaka, G. Kawano, and H. Tsukagoshi, "Long-mover: Flexible Tube In-pipe Inspection Robot for Long Distance and Complex Piping," en, in *2018 IEEE/ASME International Conference on Advanced Intelligent Mechatronics (AIM)*, Auckland: IEEE, Jul. 2018, pp. 1075–1080.
- [25] K. Hayashi, T. Akagi, S. Dohta, et al., "Improvement of Pipe Holding Mechanism and Inchworm Type Flexible Pipe Inspection Robot," en, *International Journal of Mechanical Engineering and Robotics Research*, pp. 894–899, 2020.
- [26] C. Luedtke, X. Zhou, and X. Tan, "A 3D-Printed Worm-Like Robot for Corrugated Pipes Using Anisotropic Fins," en, *IEEE/ASME Transactions on Mechatronics*, pp. 1–8, 2025.
- [27] Y. Lin, Y.-X. Xu, and J.-Y. Juang, "Single-Actuator Soft Robot for In-Pipe Crawling," en, *Soft Robotics*, vol. 10, no. 1, pp. 174–186, Feb. 2023.
- [28] *Pneumatic Artificial Muscles*, en. [Online]. Available: <https://softroboticstoolkit.com/book/pneumatic-artificial-muscles> (visited on 07/10/2025).
- [29] M. G. Selvamuthu, R. Tadakuma, N. Fujiwara, et al., "Development of soft inchworm robot with friction control of feet using double-network gel," en, *Advanced Robotics*, vol. 37, no. 6, pp. 407–422, Mar. 2023.
- [30] S. Thomas, P. Germano, T. Martinez, and Y. Perriard, "An untethered mechanically-intelligent inchworm robot powered by a shape memory alloy oscillator," en, *Sensors and Actuators A: Physical*, vol. 332, p. 113 115, Dec. 2021, Publisher: Elsevier BV.
- [31] *Smart Wire (Smart Material)*, en-gb. [Online]. Available: <https://www.philipharris.co.uk/product/chemistry/materials-and-their-properties/smart-materials/smart-wire-smart-material/pp00054321> (visited on 07/10/2025).
- [32] Q. Xie, S. Liu, and X. Ma, "Design of a novel inchworm in-pipe robot based on cam-linkage mechanism," en, *Advances in Mechanical Engineering*, vol. 13, no. 9, p. 16 878 140 211 045 193, Sep. 2021.
- [33] W. Saab, P. Racioppo, A. Kumar, and P. Ben-Tzvi, "Design of a miniature modular inchworm robot with an anisotropic friction skin," en, *Robotica*, vol. 37, no. 3, pp. 521–538, Mar. 2019, Publisher: Cambridge University Press (CUP).

- [34] Robert L. Norton, "Design of machinery: An introduction to the synthesis and analysis of mechanisms and machines," en, *Choice Reviews Online*, vol. 30, no. 03, pp. 30–1544–30–1544, Nov. 1992, Publisher: American Library Association.
- [35] *Anisotropy - an overview — ScienceDirect Topics*. [Online]. Available: <https://www.sciencedirect.com/topics/neuroscience/anisotropy#> (visited on 07/01/2025).
- [36] A. Rafsanjani, Y. Zhang, B. Liu, S. M. Rubinstei, and K. Bertoldi, "Kirigami skins make a simple soft actuator crawl," *Science Robotics*, vol. 3, no. 15, eaar7555, Feb. 2018, Publisher: American Association for the Advancement of Science.
- [37] *Pipebots*, en. [Online]. Available: <https://pipebots.ac.uk/> (visited on 07/01/2025).
- [38] *Tough 2000 Resin*, en. [Online]. Available: https://formlabs.com/uk/store/materials/tough-2000-resin/?srsltid=AfmB0oq60g7aYRfWPrMmMPOLQCvQ_YAQl8GDj1jgxMezckl08MoY4q9k (visited on 07/26/2025).
- [39] Chennu Vinodh Reddy et al, *Cams, Followers and their Types*. [Online]. Available: <https://www.mechanicalengineering.blog/2024/12/cams-followers-types.html>.
- [40] Yi Zhang, *Chapter 6. Cams*. [Online]. Available: <https://www.cs.cmu.edu/~rapidproto/mechanisms/chpt6.html> (visited on 07/11/2025).
- [41] H. A. Rothbart, Ed., *Cam design handbook*, en. New York: McGraw-Hill, 2004.
- [42] *Welcome to Python.org*, en, Jul. 2025. [Online]. Available: <https://www.python.org/> (visited on 07/22/2025).
- [43] *Autodesk Fusion — 3D CAD, CAM, CAE, & PCB Cloud-Based Software — Autodesk*, en-GB. [Online]. Available: <https://www.autodesk.com/uk/products/fusion-360/overview> (visited on 07/22/2025).
- [44] J. Briot, *JeromeBriot/fusion360-import-spline-any-csv*, original-date: 2023-01-26T17:17:34Z, Jul. 2025. [Online]. Available: <https://github.com/JeromeBriot/fusion360-import-spline-any-csv> (visited on 07/22/2025).
- [45] G. Boothroyd, P. Dewhurst, and W. A. Knight, *Product design for manufacture and assembly* (Manufacturing engineering and materials processing 58), en, 2nd ed., rev. and expanded. New York: Marcel Dekker, 2002.
- [46] *6 Alternatives to 3D Printing*, en-us. [Online]. Available: <https://www.xometry.com/resources/3d-printing/3d-printing-alternatives/> (visited on 07/23/2025).
- [47] *Best 3D Printing Filament for Functional Parts — Bambu Lab*, en. [Online]. Available: <https://bambulab.com/en/filament/collections/functional-parts> (visited on 07/24/2025).
- [48] *18V XR Brushless Compact Drill Driver (2 X 2 Ah) — DEWALT*, en. [Online]. Available: <https://www.dewalt.co.uk/product/dcd777d2t-gb/18v-xr-brushless-compact-drill-driver-2-x-2-ah> (visited on 07/24/2025).
- [49] Polulu, *Polulu Micro Metal Gear Motors*. [Online]. Available: <https://www.pololu.com/file/0J1487/pololu-micro-metal-gearmotors-rev-6-1.pdf>.
- [50] *Mecmesin — Force and Torque Testing Solutions*, en. [Online]. Available: <https://www.mecmesin.com/> (visited on 07/29/2025).
- [51] Xencast, *PX30 Resin*. [Online]. Available: <https://www.easycomposites.co.uk/xencast-px30-soft-flexible-polyurethane-rubber>.
- [52] *RS PRO RSDM3055 Bench Digital Multimeter, True RMS, 10A ac Max, 10A dc Max, 750V ac Max — RS*. [Online]. Available: <https://uk.rs-online.com/web/p/multimeters/1236465> (visited on 08/13/2025).
- [53] W. Saab, A. Kumar, and P. Ben-Tzvi, "Design and Analysis of a Miniature Modular Inch-worm Robot," en, in *Volume 5A: 40th Mechanisms and Robotics Conference*, Charlotte, North Carolina, USA: American Society of Mechanical Engineers, Aug. 2016, V05AT07A060.

A Integrated Linear Bearing Testing

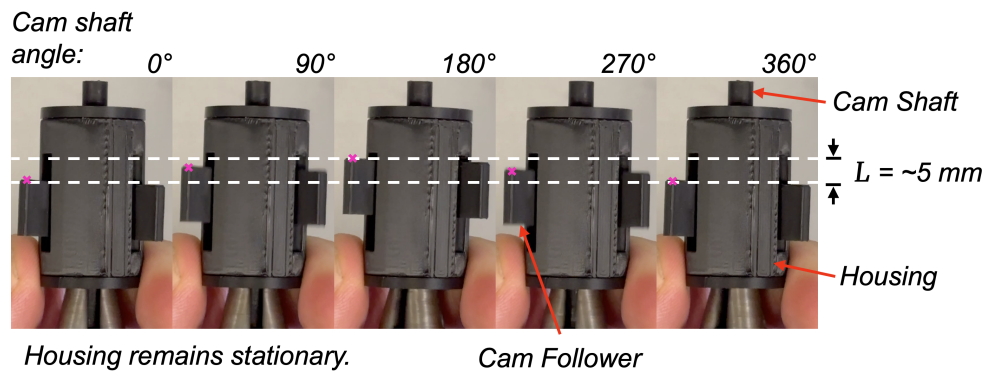


Figure A.1: Testing the linear bearing subassembly. The cam shaft is rotated, causing the cam follower to reciprocate, whilst the housing remains stationary.

B Inchworm Prototype Assembly

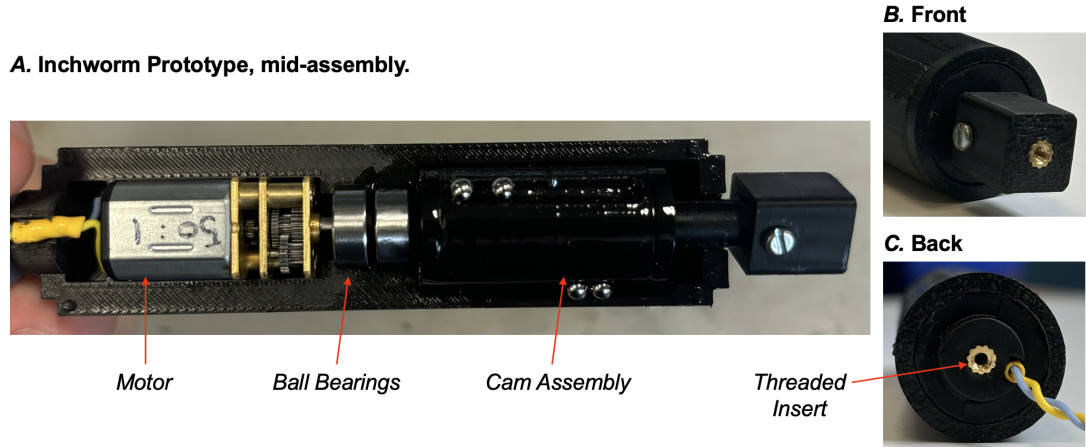


Figure B.1: (A) The inchworm mid-assembly. (B,C) Threaded inserts for attaching bristle assemblies.

C Slipping Bristles

Figure C.1 illustrates a bristle assembly slipping during the elongation phase of inch-worm locomotion.

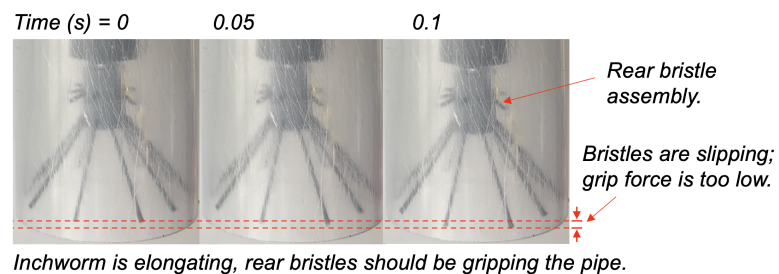


Figure C.1: Bristle assemblies slipping during the elongation phase.

D Cam Curve Comparison

This section contains Cam Path Generator output for 3 different cam curves: A DRDR cycloidal curve (used in this project), an RR sine squared curve Equation D.1, and an RR polynomial curve Equation D.2.

D.1 Sine Squared

The RR sine squared displacement equation is shown below. SVAJ plot is shown in Figure D.1.

$$s = \sin^2(u) \quad (\text{D.1})$$

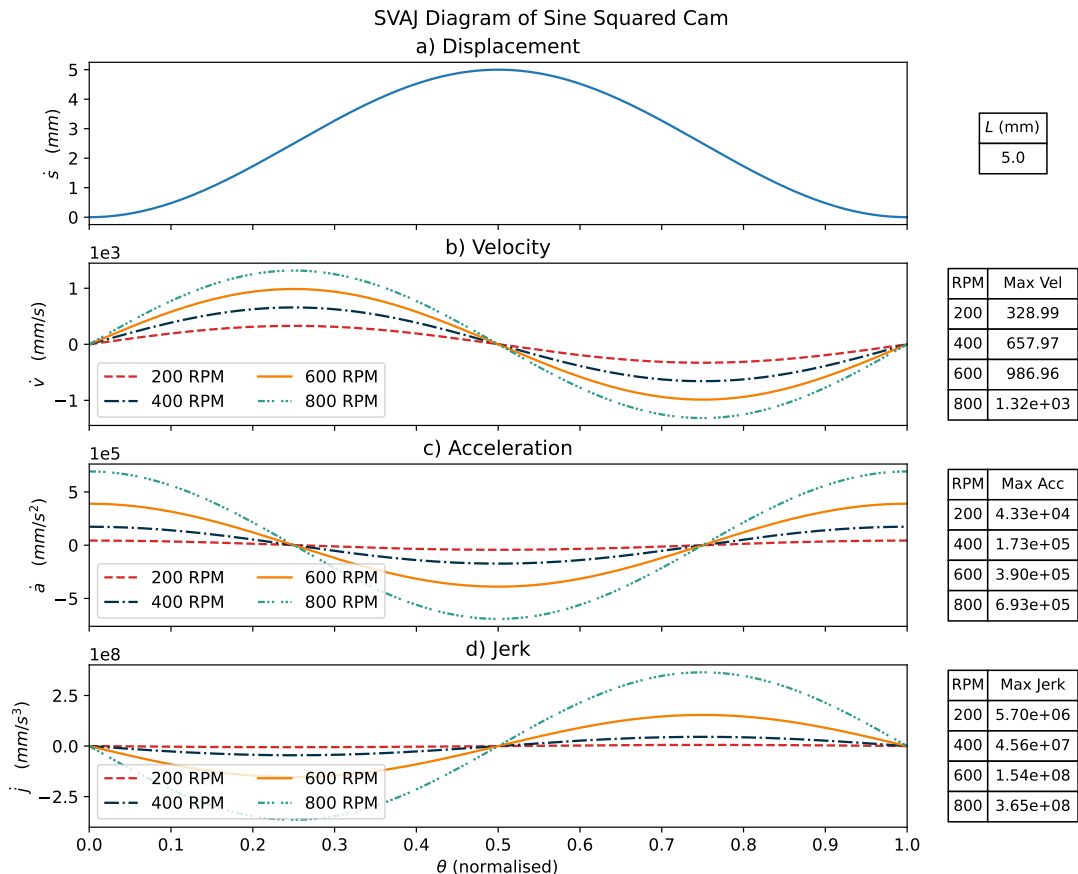


Figure D.1: Sine Square Cam SVAJ.

D.2 Polynomial Cam Curve

The RR polynomial cam curve, taken from [34], is shown in the SVAJ plot in Figure D.2.

$$s = 64 \times u^3 - 192 \times u^4 + 192 \times u^5 - 64 \times u^6 \quad (\text{D.2})$$

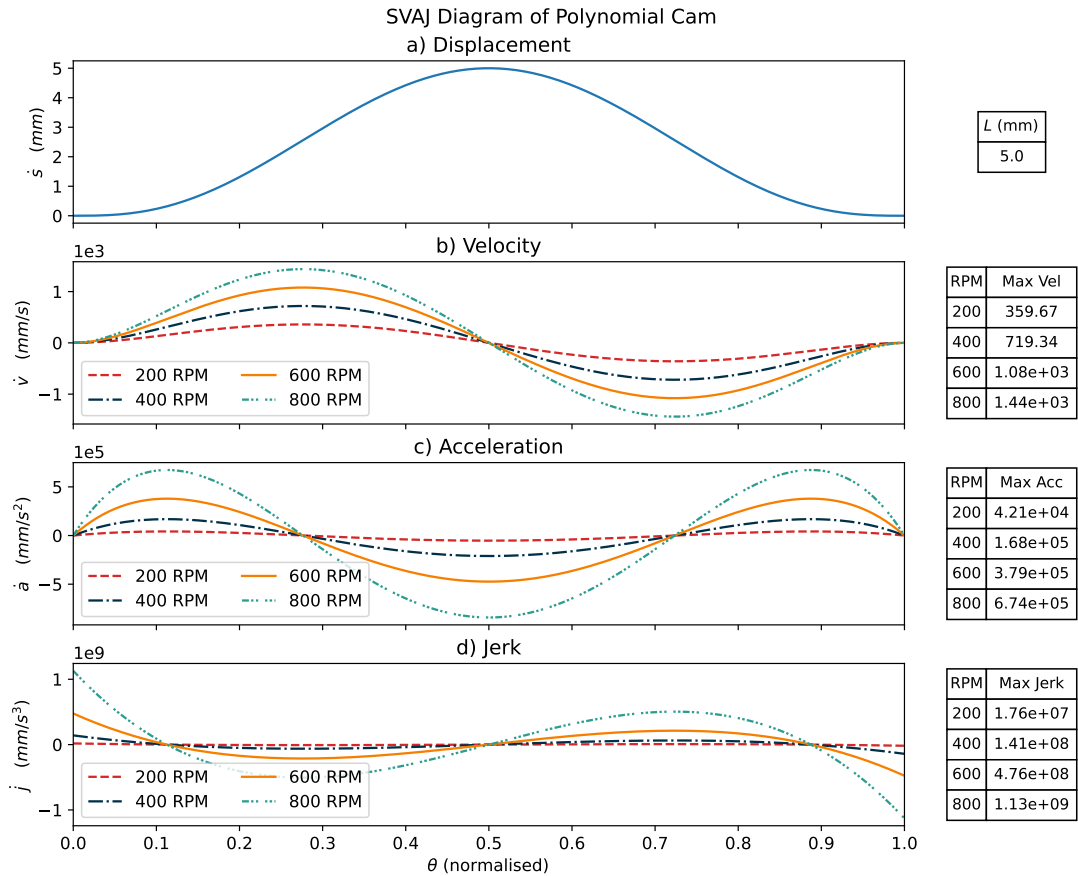


Figure D.2: Polynomial Cam SVAJ.

E Inchworm Comparison

Table E.1 shows a comparison of the cam-based inchworm against the inchworm robots featured in the literature review (section 2.4). The cam-based inchworm robot achieved the highest maximum velocity of the robots capable of traversing < 50 mm internal diameter pipes. When equipped with the optimal motor (motor C), the robot is estimated to achieve a maximum velocity of 37.2 mm s^{-1} .

Inchworm Robot	Actuation Type	Diameter < 50 mm?	Max Velocity (mm s^{-1})	Rank
Saab et al [53]	Crank and Slider	No	138.0	–
Lin et al [27]	McKibben (pneumatic)	No	27.0	–
Miyasaka et al [24]	Pneumatic	Yes	24.2	2
Hayashi et al [25]	Pneumatic	Yes	14.0	3
Peng et al [8]	Pneumatic	Yes	8.5	4
Luedtke et al [26]	Pneumatic	Yes	4.4	5
Wang et al [21]	SMA	Yes	3.5	6
This Research	Cylindrical Cam	Yes	25.5	1
This Research				
Original Prototype	Cylindrical Cam	Yes	12.23	–
Optimised Bristles	Cylindrical Cam	Yes	25.50	1
Optimised Motor	Cylindrical Cam	Yes	37.24	–

Table E.1: Comparison of the cam-based inchworm robot against other inchworms in the literature.

F Cam Path Generator Software

Source code for the cam path generator software can be found at:
<https://github.com/tom-milner/PipeRobot.git>.